

RESEARCH ARTICLE

10.1002/2013JE004476

Key Points:

- The crystalline plagioclase absorption is examined across the lunar surface
- Pure plagioclase is overwhelmingly concentrated around impact basins
- The thickness of primary anorthositic crust was at least 30 km thick

Supporting Information:

- Readme
- Table S1
- Figure S1

Correspondence to:

K. L. Donaldson Hanna,
kerri_donaldson_hanna@brown.edu

Citation:

Donaldson Hanna, K. L., L. C. Cheek, C. M. Pieters, J. F. Mustard, B. T. Greenhagen, I. R. Thomas, and N. E. Bowles (2014), Global assessment of pure crystalline plagioclase across the Moon and implications for the evolution of the primary crust, *J. Geophys. Res. Planets*, 119, doi:10.1002/2013JE004476.

Received 27 JUN 2013

Accepted 26 APR 2014

Accepted article online 30 APR 2014

Global assessment of pure crystalline plagioclase across the Moon and implications for the evolution of the primary crust

K. L. Donaldson Hanna¹, L. C. Cheek¹, C. M. Pieters¹, J. F. Mustard¹, B. T. Greenhagen², I. R. Thomas³, and N. E. Bowles³
¹Department of Geological Sciences, Brown University, Providence, Rhode Island, USA, ²Jet Propulsion Laboratory, California Institute of Technology, Pasadena, California, USA, ³Atmospheric, Oceanic, and Planetary Physics, University of Oxford, Oxford, UK

Abstract Recent advancements in visible to near infrared orbital measurements of the lunar surface have allowed the character and extent of the primary anorthositic crust to be studied at unprecedented spatial and spectral resolutions. Here we assess the lunar primary anorthositic crust in global context using a spectral parameter tool for Moon Mineralogy Mapper data to identify and map Fe-bearing crystalline plagioclase based on its diagnostic 1.25 μm absorption band. This allows plagioclase-dominated rocks, specifically anorthosites, to be unambiguously identified as well as distinguished from lithologies with minor to trace amounts of mafic minerals. Low spatial resolution global mosaics and high spatial resolution individual data strips covering more than 650 targeted craters were analyzed to identify and map the mineralogy of spectrally pure regions as small as ~ 400 m in size. Spectrally, pure plagioclase is identified in approximately 450 targets located across the lunar surface. Diviner thermal infrared (TIR) data are analyzed for 37 of these nearly monomineralic regions in order to understand the compositional variability of plagioclase (An#) in these areas. The average An# for each spectrally pure region is estimated using new laboratory measurements of a well-characterized anorthite (An₉₆) sample. Diviner TIR results suggest that the plagioclase composition across the lunar highlands is relatively uniform, high in calcium content, and consistent with plagioclase compositions found in the ferroan anorthosites (An_{94–98}). Our results confirm that spectrally pure anorthosite is widely distributed across the lunar surface, and most exposures of the ancient anorthositic crust are concentrated in regions of thicker crust surrounding impact basins on the lunar nearside and farside. In addition, the scale of the impact basins and the global nature and distribution of pure plagioclase requires a coherent zone of anorthosite of similar composition in the lunar crust supporting its formation from a single differentiation event like a magma ocean. Our identifications of pure anorthosite combined with the GRAIL crustal thickness model suggest that pure anorthosite is currently observed at a range of crustal thickness values between 9 and 63 km and that the primary anorthositic crust must have been at least 30 km thick.

1. Introduction

It is hypothesized that the anorthositic highlands, the primary crust of the Moon, formed by the crystallization and flotation of plagioclase in the late stages of a lunar magma ocean due to the density difference between plagioclase and the remaining mafic liquid [e.g., Smith *et al.*, 1970; Wood *et al.*, 1970; Ryder, 1982; Warren, 1985, 1990]. The impetus for these magma ocean models came from the analyses of pristine samples returned from the Apollo missions. The first evidence of the lunar primary crust came in the form of a specific rock type, the ferroan anorthosite (FAN), which was distributed among the samples from the Apollo 11, 15, and 16 landing sites [e.g., Wood *et al.*, 1970; Dowty *et al.*, 1974]. The ferroan anorthosites have distinct characteristics that uniquely identify them from other pristine rock samples. In particular, plagioclase in FANs has a small compositional range (An_{94–98}), while the minor mafic minerals found in association with plagioclase in this rock type are ferroan relative to the mafic components of other pristine lunar rocks (Mg_{35–75}) [e.g., Dowty *et al.*, 1974; Warren, 1985; McGee, 1993; Papike *et al.*, 1996]. A single, global differentiation event was invoked to account for the observed compositional trend and the wide geographic distribution of FANs among the Apollo samples. However, it is unclear how representative the FANs are of the anorthositic highlands, as another type of anorthosite, the magnesian anorthosites (An_{95–97} and Mg_{75–85}),

has been identified in lunar breccias [James *et al.*, 1989] and feldspathic meteorites [e.g., Korotev *et al.*, 2003; Takeda *et al.*, 2006; Gross *et al.*, 2012]. Various models involving serial magmatism have been suggested as the formation mechanism for both ferroan and magnesian anorthosites [e.g., Wetherill, 1975; Longhi and Ashwal, 1985; Longhi, 2003; Gross *et al.*, 2012] and recently Ohtake *et al.* [2012] suggested asymmetric crustal growth within a lunar magma ocean to explain the formation of the two types of anorthosites. To gain a better understanding of the lunar crust's formation mechanism, it is important to first understand the crystalline nature, composition, geologic setting, and distribution of primary anorthositic crust exposed at the lunar surface.

Early telescopic observations and orbital measurements of the lunar surface from the Clementine UV visible camera and the Galileo solid-state imager identified exposures thought to be evidence of the Moon's primary anorthositic crust around the inner rings of lunar basins [e.g., Spudis *et al.*, 1984; Hawke *et al.*, 1985, 1991, 2003; Peterson *et al.*, 1995, 1996, 1997; Bussey and Spudis, 2000], in the central peaks of complex craters associated with the outer rings of lunar basins [e.g., Pieters, 1986; Coombs *et al.*, 1990; Hawke *et al.*, 2003], and at northern latitudes on the farside [e.g., Peterson *et al.*, 1996, 1997; Hawke *et al.*, 2003]. Near infrared (NIR) Earth-based telescopic observations identified regions on the lunar surface with spectral characteristics (featureless, high-albedo spectra) believed to be consistent with shocked or noncrystalline plagioclase [e.g., Spudis *et al.*, 1984; Pieters, 1986; Hawke *et al.*, 1991, 2003; Peterson *et al.*, 1995]. A few select areas exhibited hints of a 1.25 μm absorption band diagnostic of Fe-bearing crystalline plagioclase [Hawke *et al.*, 1985; Coombs *et al.*, 1990], but the elusive absorption was difficult to confirm. Early Clementine and Galileo multispectral imagery data and FeO and TiO₂ abundance estimates based on multispectral imagery [Lucey *et al.*, 1995, 1998; Blewett *et al.*, 1997] were used to identify regions of anorthosite based on high-albedo values, very low FeO and TiO₂ abundances, and low values for band ratios sensitive to the presence of mafic minerals [e.g., Peterson *et al.*, 1996, 1997; Bussey and Spudis, 2000]. Thus, due to spatial and spectral resolution limits, most early identifications of anorthosite were based on the *absence* of mafic mineral diagnostic absorption bands in NIR spectral measurements, not by the presence of a diagnostic absorption band for Fe-bearing crystalline plagioclase.

Recently, the Moon's surface has been mapped at high spatial (20 to 500 m/pixel) and high spectral (9 to 296 spectral bands) resolution by NIR imaging spectrometers onboard the SELENE and Chandrayaan-1 spacecraft [e.g., Kato *et al.*, 2008; Ohtake *et al.*, 2008; Pieters *et al.*, 2009b; Boardman *et al.*, 2011; Green *et al.*, 2011]. These combined technological improvements have allowed the SELENE Spectral Profiler and Multiband Imager (MI) and the Chandrayaan-1 Moon Mineralogy Mapper (M³) to unambiguously identify Fe-bearing crystalline plagioclase across the lunar surface based on its unique 1.25 μm absorption band [Burns, 1970, 1993; Adams and McCord, 1971a; Adams and Goullaud, 1978]. Pure crystalline plagioclase has now been identified in widespread locations across the lunar surface: around impact basins, in massifs in the Inner Rook Mountains of Orientale, and in the central peaks, walls, floor, and ejecta of craters [Matsunaga *et al.*, 2008; Ohtake *et al.*, 2009; Pieters *et al.*, 2009a; Dhingra *et al.*, 2011; Donaldson Hanna *et al.*, 2012a; Yamamoto *et al.*, 2012; Cheek *et al.*, 2013]. While previous NIR laboratory studies have suggested that the band depth and center position of the 1.25 μm feature may vary with Fe and An contents [Bell and Mao, 1973; Adams and Goullaud, 1978; Cheek *et al.*, 2009, 2011], the relationship between NIR spectral properties of plagioclase and its composition (An#) has yet to be quantified. However, new laboratory thermal infrared (TIR) emissivity measurements of varying compositions of the plagioclase solid solution series measured under simulated lunar conditions demonstrate that the position of the Christiansen feature (CF), an emissivity maximum indicative of composition [Conel, 1969], can be linearly related to the An# [Donaldson Hanna *et al.*, 2012b]. Ca-rich plagioclase compositions like anorthite have CF positions near 7.84 μm , while Na-rich compositions like albite have CF positions near 7.52 μm . Thus, the regions of spectrally pure crystalline plagioclase (<1% olivine and pyroxene) as identified in NIR spectra are ideal areas to investigate the utility of TIR data to constrain plagioclase compositions [Greenhagen *et al.*, 2010].

In this work, we describe the spectral parameter developed as a tool to specifically highlight Fe-bearing crystalline plagioclase from mafic minerals with absorption bands at similar or overlapping wavelengths to the plagioclase absorption band. Using this new spectral parameter as a tool for investigation, we (1) globally map the exposures of Fe-bearing crystalline plagioclase, (2) estimate the purity of these exposures, and (3) identify nearby lithologies. Additionally, we use the thermal infrared observations of the identified spectrally pure plagioclase regions to estimate the compositional variability of plagioclase across the lunar highlands.

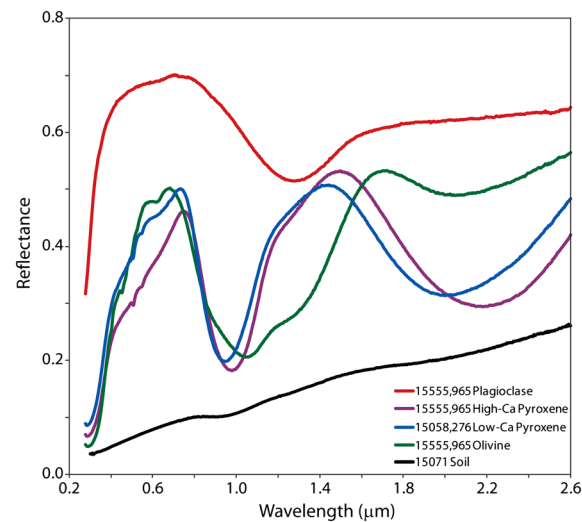


Figure 1. Reflectance Experiment Laboratory's visible to near infrared reflectance spectra of hand-separated mineral separates from mare basalts 15555,965 and 15058,276 [Isaacson *et al.*, 2011] as well as lunar soil 15071 Pieters *et al.* [2000]. Spectral measurements are of the $<45\ \mu\text{m}$ particle size fraction. Diagnostic absorption bands near 1, 1.25, and $2\ \mu\text{m}$ are due to electronic transitions of Fe^{2+} in the crystal structures of plagioclase, pyroxene, and olivine.

We document and discuss the composition, character, and distribution of pure anorthosites across the lunar surface as well as the implications these exposures have on the formation and evolution of the Moon's primary anorthositic crust.

2. Background

2.1. Near Infrared Spectroscopy

Spectral measurements at NIR wavelengths identify Fe-bearing minerals such as pyroxene, olivine, and plagioclase by using broad absorptions at characteristic wavelengths caused by electronic transitions of Fe^{2+} in specific crystal structures as seen in Figure 1. Pyroxenes have diagnostic absorption bands near 1 and $2\ \mu\text{m}$ with the position of the bands being dependent on the composition of pyroxene according to Mg number and Ca content [Burns, 1970, 1993; Adams, 1974; Hazen *et al.*, 1978; Klima *et al.*, 2007, 2011]. Olivine has three overlapping absorptions between 0.9 and $1.25\ \mu\text{m}$, and these absorptions shift to longer wavelengths as the Fe content increases [Burns,

1970, 1993; Sunshine and Pieters, 1998]. The identification of Fe-bearing crystalline plagioclase in the NIR is based on a broad absorption band at approximately $1.25\ \mu\text{m}$ due to minor amounts of Fe^{2+} being incorporated into the crystal structure. Laboratory studies of plagioclase has shown that only $\sim 0.1\ \text{wt}\%$ of FeO is needed to generate an absorption band and the band depth and center position of the diagnostic $1.25\ \mu\text{m}$ band may vary with Fe abundance and An#, respectively [Adams and McCord, 1971a; Bell and Mao, 1973; Adams and Goullaud, 1978; Cheek *et al.*, 2009, 2011].

The strength of plagioclase's diagnostic absorption at $1.25\ \mu\text{m}$ can be weakened, to the point of disappearance, by at least two known surface processes: space weathering and shock metamorphism. The extensive fracturing and change in effective grain size that occur as a result of impacts are also likely to play a role. Exposed rocks and soils in the lunar regolith are bombarded relentlessly by energetic micrometeorites that comminute, vaporize, melt, and fuse surface materials. In addition, during the energetic impact process, metallic nanophase iron (npFe⁰) is formed [Noble *et al.*, 2001]. This npFe⁰ is observed in inclusion-rich rims formed on the surface of lunar soil grains from the deposition of impact-generated vapors with contribution from solar wind sputtered ions [Keller and McKay, 1997] and is incorporated into the interiors of agglutinitic glasses [Keller *et al.*, 1998]. The abundance of npFe⁰ in the regolith depends on the length of time the surface has been exposed to weathering, the abundance of FeO in the original rocks and minerals, and the energy of impacting meteorites. The accumulation of npFe⁰ over time changes the optical properties of the soil and affects near infrared reflectance spectra in several well-characterized ways: lower albedos, weaker absorption bands, and often a red sloped spectrum (decreased reflectance at shorter wavelengths) [e.g., Adams and McCord, 1970; Adams and McCord, 1971b; Pieters *et al.*, 1993; Pieters *et al.*, 2000; Hapke, 2001]. In Figure 1, a spectrum of Apollo 15 soil 15071 is shown along with pure mineral separates to illustrate the spectral effects due to space weathering.

Shock metamorphism owing to larger-scale impacts can also diminish the diagnostic absorption band near $1.25\ \mu\text{m}$. At shock pressures between ~ 10 and $30\ \text{GPa}$, mineral crystals are fractured, broken into smaller blocks, and internally fragmented [e.g., von Engelhardt *et al.*, 1967; von Engelhardt and Stöffler, 1968; Stöffler, 1971; Hörz and Quaide, 1973; Gibbons and Ahrens, 1977]. This deformation to the crystal structure increases the scattering of light effectively decreasing the path length for photons to pass through the mineral grain, thus weakening the diagnostic absorption band. At shock pressures near $\sim 25\ \text{GPa}$, plagioclase begins to lose

its crystal structure and diaplectic glass starts to form, and by ~35 GPa, 100% of the plagioclase has been transformed to diaplectic glass, or maskelynite [von Engelhardt *et al.*, 1967; von Engelhardt and Stöffler, 1968; Stöffler, 1971; Gibbons and Ahrens, 1977]. As maskelynite is amorphous, it does not have the crystal structure for electronic transitions of Fe^{2+} needed to produce plagioclase diagnostic absorption bands. As the amount of maskelynite increases, the 1.25 μm absorption band widens and weakens as seen in plagioclase shocked naturally [Adams *et al.*, 1979; Bruckenthal and Pieters, 1984] and in the laboratory [Johnson and Hörz, 2003]. If maskelynite is subsequently unaffected by the fracturing and fragmental effects of shock, it exhibits a weak ferrous absorption near 1 μm [Pieters, 1996].

Lucey [2002] used a nonlinear radiative transfer technique to illustrate that NIR spectra assumed to be shocked plagioclase from Orientale [Spudis *et al.*, 1984] could be modeled with either crystalline anorthite plus npFe^0 or shocked anorthite and get similar spectral results. Thus, to uniquely distinguish shocked plagioclase outcrops from space weathered soils, additional information such as albedo and the geologic context should be explored using high spatial resolution imagery like the Lunar Reconnaissance Orbiter Camera or the Kaguya Terrain Camera [Dhingra *et al.*, 2011]. To avoid the ambiguity between shocked versus weathered regions, our study focuses only on regions that clearly exhibit the 1.25 μm absorption band resulting from minor amounts of Fe^{2+} in crystalline plagioclase and are unambiguously rich in Fe-bearing plagioclase.

2.2. Thermal Infrared Spectroscopy

As seen in Figure 3, TIR spectra of fine particulate samples have diagnostic features indicative of rock and mineral compositions. These include (1) the CF, an emissivity maximum resulting from a rapid change in the refractive index at wavelengths just short of the fundamental molecular vibration bands; (2) the reststrahlen bands (RB), emissivity absorptions (minima) due to the fundamental molecular vibrations; and (3) the transparency feature (TF), an emissivity minimum in the relatively transparent spectral region (low absorption coefficients) between the principal RB due to particle sizes on the order of the wavelength of light and volume scattering lowering the emittance across this spectral region [Salisbury and Walter, 1989]. Conel [1969] found that the CF in silicates is diagnostic of mineralogy and average composition and changes with the change in bond strength and molecular geometry associated with changing mineralogy. Of the known silicate minerals on the Moon, plagioclase feldspars, which have little Fe and higher Al and Ca contents, have shorter wavelength CF positions than pyroxenes and olivines, which have higher Fe and/or Mg contents and no Al. In addition, laboratory work by Nash and Salisbury [1991] demonstrated that the wavelength position of the CF can also be used to distinguish between plagioclase compositions (An#), as Ca-rich plagioclase (anorthite) has a longer CF position than Na-rich plagioclase (albite). The vibrational characteristics of the RB (exact frequencies, shapes and intensities, and number of absorptions) are dependent on atomic masses, geometry between atoms, and their bond strengths, which are determined by the arrangement of the anions in the crystal structure as well as the location and composition of the cations associated with them. As all minerals consist of unique structures and/or compositions, virtually, every mineral has a different suite of vibrational characteristics and thus a unique set of RB absorptions [e.g., Lyon, 1964; Conel, 1969; Salisbury and Walter, 1989]. TF, like the CF, are indicators of mineral compositions, and there is a higher probability of determining specific rock type compositions if both the CF and TF are used for interpretations [Salisbury and Walter, 1989; Cooper *et al.*, 2002]. As particles decrease in size, the spectral contrast of the TF increases.

In the vacuum, near-surface environment of airless bodies like the Moon and asteroids, there are no interstitial gases between regolith grains to transfer heat via conduction. Thus, radiative cooling dominates and a thermal gradient in the upper hundred microns of regolith is created. Laboratory studies of particulate rocks and minerals as well as selected lunar soils under vacuum and lunar-like conditions have identified significant effects of this thermal gradient on TIR spectral measurements [e.g., Logan *et al.*, 1973; Salisbury and Walter, 1989; Henderson *et al.*, 1996; Thomas *et al.*, 2012; Donaldson Hanna *et al.*, 2012b]. As seen in TIR spectra of Miyake-jima anorthite (An_{96}) [e.g., Kimata *et al.*, 1995; Amma-Miyasaka and Nakagawa, 2002] measured under simulated lunar conditions in the Simulated Lunar Environment Chamber at the University of Oxford [Thomas *et al.*, 2012] in Figure 4, these spectral effects include (1) the CF shifts to shorter wavelengths from 8.11 μm (1233 cm^{-1}) to 7.84 μm (1275 cm^{-1}), (2) the spectral contrast of the CF relative to the RB increases, and (3) the TF disappears as it does for most silicate minerals measured under simulated lunar conditions. Recent laboratory studies of well-characterized plagioclase samples have also demonstrated that the

wavelength position of the CF measured under simulated lunar conditions can still be used to distinguish between plagioclase compositions (An#), as the CF shifts systematically to shorter wavelengths (higher wave numbers), as the Ca content, or An# decreases, [Donaldson Hanna *et al.*, 2012c].

Another consideration for the interpretation of TIR data sets is the effects of space weathering on TIR emissivity spectra. Early laboratory studies on plagioclase feldspars suggested that the wavelength position of the CF is not affected by the vitrification of the lunar surface [Nash and Salisbury, 1991]. However, the effects due to the accumulation of nanophase iron (npFe⁰) were not investigated. Recent TIR measurements of the lunar surface by the Diviner Lunar Radiometer Experiment suggest that space weathering does affect the wavelength position of the CF. Young fresh craters, like Tycho, show anomalous CF values relative to their surrounding terrain. The CF values for these fresh surfaces appear at shorter wavelengths than the CF value for the surrounding materials. Thus, space weathering appears to systematically shift the CF value toward longer wavelengths by ~0.1 μm with increasing maturity [Greenhagen *et al.*, 2010; Lucey *et al.*, 2010, 2013]. The source(s) of this observed shift and the degree of this shift is still under investigation. However, in this study we focus only on regions that clearly exhibit the 1.25 μm absorption band suggesting space weathering should have little effect on the Diviner measurements of the investigated regions.

3. Data and Methods

3.1. Moon Mineralogy Mapper

The Moon Mineralogy Mapper (M³) is an imaging spectrometer launched onboard the Indian Space Research Organization's Chandrayaan-1 and successfully acquired spectral "image cubes" of the global lunar surface across 85 wavelengths (0.43–3.0 μm) at a spatial resolution of 140 or 280 m/pixel (depending on the spacecraft's altitude) [Green *et al.*, 2011]. In this analysis, two types of M³ reflectance data are used: (1) individual high spatial resolution data strips and (2) lower spatial resolution global mosaics of M³ data prepared for each of the instrument's optical periods [Boardman *et al.*, 2011]. The hot and cold ground truth corrections [Lundeen *et al.*, 2011; Isaacson *et al.*, 2013] were applied to the level 2 reflectance data depending on the observing conditions for each M³ strip.

A spectral parameter was developed for M³ data to specifically highlight areas that exhibit a prominent 1.25 μm absorption band due to plagioclase. An integrated band depth (1.25IBD) of the 1.25 μm absorption band was calculated by removing a continuum between 1.03 and 1.7 μm and summing band depths over 27 spectral bands across the broad 1.25 μm absorption. The equation used to calculate the 1.25IBD is

$$\sum_{n=0}^{26} 1 - R(1029 + 20n)/R_c(1029 + 20n),$$

where 1029 is the first wavelength (in nanometers) of the continuum,

20 is the wavelength step size in nanometers, n is the number of spectral bands to be integrated across, R is the reflectance value at the given wavelength, and R_c is the continuum reflectance at the same given wavelength. The end points of the continuum as well as the spectral bands included in the 1.25IBD calculations were chosen in a portion of the spectrum that would maximize contributions from the crystalline plagioclase band while limiting the contribution from pyroxene and olivine bands to the integrated band depth. Figure 2 illustrates the method for calculating the 1.25IBD for crystalline plagioclase and "featureless" spectra. Clearly, pixels exhibiting spectra with prominent Fe-bearing crystalline plagioclase absorptions will have higher 1.25IBD values while pixels with featureless spectra have lower 1.25IBD values. Pixels classified as having "high" values correlate to spectra with 1.25 μm absorption band strengths >1–2%. Spectra are classified as featureless if they have "low" 1.25IBD values and lack perceptible (spectral contrast < 1–2%) absorption features near 1, 1.25, and 2 μm. Featureless spectra could result from blocks and/or outcrops of shocked anorthosite, regions of well-developed lunar soil, or a mixture of shocked and featureless material observed at insufficient spatial resolution as discussed by Ohtake *et al.* [2013]. Further evaluation of each of those scenarios requires detailed characterization of the surface using high spatial resolution imagery like images from the Lunar Reconnaissance Orbiter Camera (LROC) Narrow Angle Camera (NAC) and is beyond the scope of this work.

The 1.25IBD spectral parameter, calculated on a pixel-by-pixel basis, was applied to the M³ data set in three different ways to investigate the global distribution of Fe-bearing crystalline plagioclase at different spatial scales. The 1.25IBD parameter was run on each of the lower resolution global mosaics [Boardman *et al.*, 2011], which allow any region larger than ~1.4 km with high 1.25IBD values to be identified. The 1.25IBD parameter

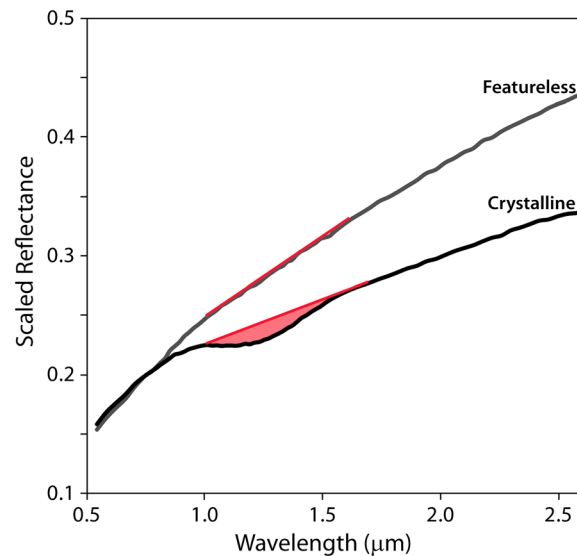


Figure 2. Typical M^3 reflectance spectra of pure crystalline plagioclase and featureless spectral units collected from Humboldt crater. Reflectance spectra are scaled at $0.75 \mu\text{m}$. The red lines indicate the continuum with tie points at 1.03 and $1.7 \mu\text{m}$ used in calculating the $1.25 \mu\text{m}$ integrated band depth (1.25IBD), and the shaded red region shows the area over which the 27 M^3 spectral bands are integrated. Featureless spectra clearly lack the diagnostic absorption band and would have a very low 1.25IBD value. Spectra are 5×5 pixel averages and are from M^3 optical period OP2C1.

was applied to M^3 full resolution mosaics generated for each optical period of all impact basin structures including protobasins, peak ring basins, and multiring basins. Additionally, the 1.25IBD parameter was calculated for individual full resolution M^3 data strips to investigate target areas that meet one or both of the following criteria: (1) all targets previously identified as rich in anorthosite [e.g., *Spudis et al.*, 1984; *Tompkins and Pieters*, 1999; *Hawke et al.*, 2003; *Matsunaga et al.*, 2008; *Ohtake et al.*, 2009; *Yamamoto et al.*, 2012] and (2) an independent catalogue of all well-characterized complex craters greater than 50 km in diameter derived from Lunar Orbiter Laser Altimeter (LOLA) data [*Head et al.*, 2010; *Fassett et al.*, 2012; *Baker et al.*, 2012]. As individual M^3 data strips are investigated for high 1.25IBD values across specific target areas, the data strips are also examined for additional high 1.25IBD pixels to identify new regions rich in Fe-bearing crystalline plagioclase. In this work, to ensure all the identifications of crystalline plagioclase are real rather than spurious pixels resulting from topography, illumination, and/or spacecraft geometry, our

identifications cover a minimum of 3–5 M^3 pixels (approximately 400–700 m) and when possible the same target was identified in multiple M^3 data strips across multiple optical periods.

M^3 spectra are extracted from each of the high 1.25IBD value regions to confirm the identification of Fe-bearing crystalline plagioclase and to estimate the “purity,” or mafic mineral abundance, of the identifications [e.g., *Cheek and Pieters*, 2012; *Cheek et al.*, 2013]. Spectra that display only a crystalline plagioclase absorption near $1.25 \mu\text{m}$ and lack mafic absorptions near 1 and $2 \mu\text{m}$ are considered “spectrally pure” plagioclase and represent anorthosites with exceedingly low-mafic mineral abundances. These spectra are referred to as pure anorthosites and correspond to Class A spectra of *Cheek et al.* [2013]. *Cheek et al.* [2013] estimated that these anorthosites contain up to ~99–100 vol % plagioclase and is similar to the designation of *Ohtake et al.* [2009], “purest anorthosite” or PAN (>98 vol %). While this M^3 global assessment of anorthosite focuses primarily on the distribution of these purest anorthosites, some of the spectra from high 1.25IBD value regions also display mafic bands that are weaker than or subequal to the crystalline plagioclase absorption creating a spectrum exhibiting multiple, but distinct features (a “w” shape). These spectra containing a weak to subequal mafic component are referred to as “nonpure” anorthosites and in most cases correspond to the Class B anorthosites from *Cheek et al.* [2013]. *Cheek et al.* [2013] estimated that these anorthosites contain up to ~96–98 vol % plagioclase, assuming that the components are in an intimate mixture.

As a significant extension of earlier studies, the combined spatial and spectral resolution of M^3 data allows for a more detailed analysis of the character and distribution of lunar anorthosites as well as the association of anorthosites with mafic mineral dominated lithologies. In each target area, where pure crystalline plagioclase is identified, other observed spectrally distinct units are classified as either mafic (olivine, pyroxene, and/or spinel) or nonpure anorthosite depending on the relative strengths of the mafic absorptions present.

3.2. Diviner Lunar Radiometer Experiment

The Diviner Lunar Radiometer Experiment (Diviner) was launched onboard the Lunar Reconnaissance Orbiter (LRO) in June 2009 and has been providing the first global coverage maps of TIR derived compositions and physical properties [e.g., *Glotch et al.*, 2010; *Greenhagen et al.*, 2010; *Paige et al.*, 2010; *Bandfield et al.*, 2011; *Allen et al.*, 2012; *Vasavada et al.*, 2012]. Diviner is a pushbroom mapping radiometer with nine channels: two

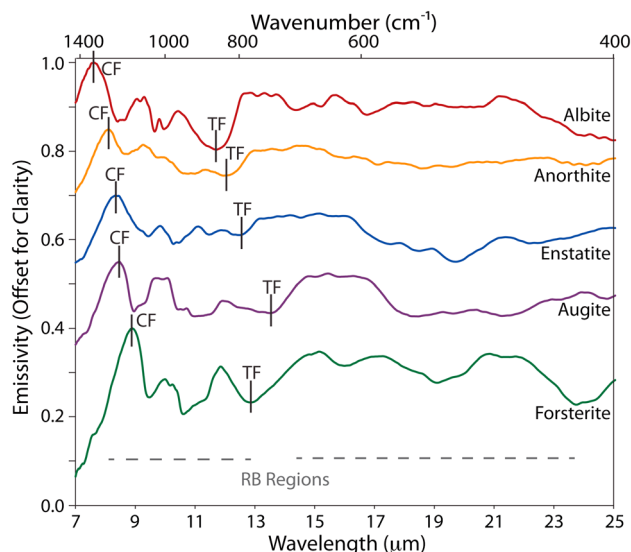


Figure 3. Full resolution laboratory spectra of fine particulate (<25 μm) silicate minerals measured under ambient conditions (samples are heated from below to ~ 350 K and atmospheric pressure inside the chamber ~ 1000 mbar). Thermal infrared diagnostic features are labeled as follows: CF (Christiansen Feature), RB (reststrahlen bands), and TF (transparency feature). Spectra are normalized to 1.0 at a peak emission and offset by 0.15 emissivity from one another for clarity. Figure 3 is adapted from Donaldson Hanna *et al.* [2012b].

for the effects of temperature and anisothermality [Greenhagen *et al.*, 2011]. Using this method, Diviner CF maps are made for craters identified in M^3 data as containing spectrally pure plagioclase; however, we are limited by the Diviner data coverage for lunar midday over these spectrally pure plagioclase regions.

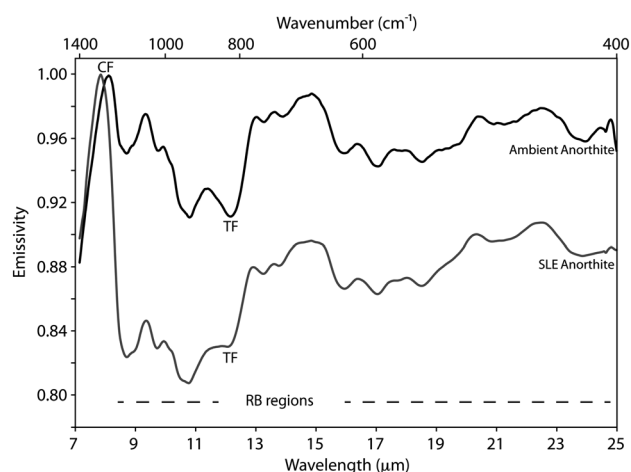


Figure 4. Fine particulate (<25 μm) Miyake-jima anorthite (An_{96}) measured under an ambient environment (black line) and simulated lunar environment (grey line) in the Simulated Lunar Environment Chamber at the University of Oxford [Thomas *et al.*, 2012]. Under ambient conditions, samples are heated from below to ~ 350 K and the chamber is filled with ~ 1000 mbar of nitrogen. Under simulated lunar conditions, samples are heated from below to ~ 350 K and heated from above using a solar-like halogen lamp while the chamber is cooled with liquid nitrogen and pressures $< 10^{-3}$ mbar. The Christiansen feature (CF), Reststrahlen bands (RB), and transparency feature (TF) are labeled.

broadband solar reflectance channels, three mineralogy channels, and four broad thermal channels and a field of view of approximately 200 m [Paige *et al.*, 2009]. Silicate mineralogy is derived from three narrow spectral channels near $8 \mu\text{m}$ (centered at 7.81 , 8.28 , and $8.55 \mu\text{m}$) that were chosen specifically to measure the peak of the CF [Greenhagen, 2009].

The silicate mineralogy of the lunar surface is characterized using the Diviner radiance data for the three channels near $8 \mu\text{m}$ for lunar midday (10:00 to 14:00 local time) that are binned and averaged at 128 pixels per degree and then converted to three point emissivity spectra as described by Greenhagen *et al.* [2010]. To approximate the wavelength position of the CF in the Diviner data, three quadratic equations are solved simultaneously to determine the wavelength of the maximum of a parabolic fit to the three point Diviner emissivity spectra. Diviner CF values are then corrected for local lunar time, latitude, and topography to account

for the effects of temperature and anisothermality [Greenhagen *et al.*, 2011]. Using this method, Diviner CF maps are made for craters identified in M^3 data as containing spectrally pure plagioclase; however, we are limited by the Diviner data coverage for lunar midday over these spectrally pure plagioclase regions. Additionally, we are limiting our analysis to craters that are $\pm 50^\circ$ from the lunar equator. At high latitudes, combining data from different times of day is not as straightforward as those at lower latitudes and can introduce larger variations in the CF value that are not necessarily real. As seen in Figure 4, the CF position for an anorthite sample (An_{96}) measured under simulated lunar conditions is $7.84 \mu\text{m}$, whereas more mafic minerals have longer wavelength CF positions. Thus, it is reasonable to assume that pixels with CF values less than $7.95 \mu\text{m}$ contain pure plagioclase when accounting for some small amount of space weathering. To further confirm the identification of plagioclase, Diviner TIR emissivity spectra are extracted. It is clear from Figures 3 and 4 that the spectra of plagioclase compositions, albite and anorthite, can be distinguished from one another as well as from the spectra of other silicate minerals.

The M^3 and Diviner data sets both use high-precision altimeter data from LRO's

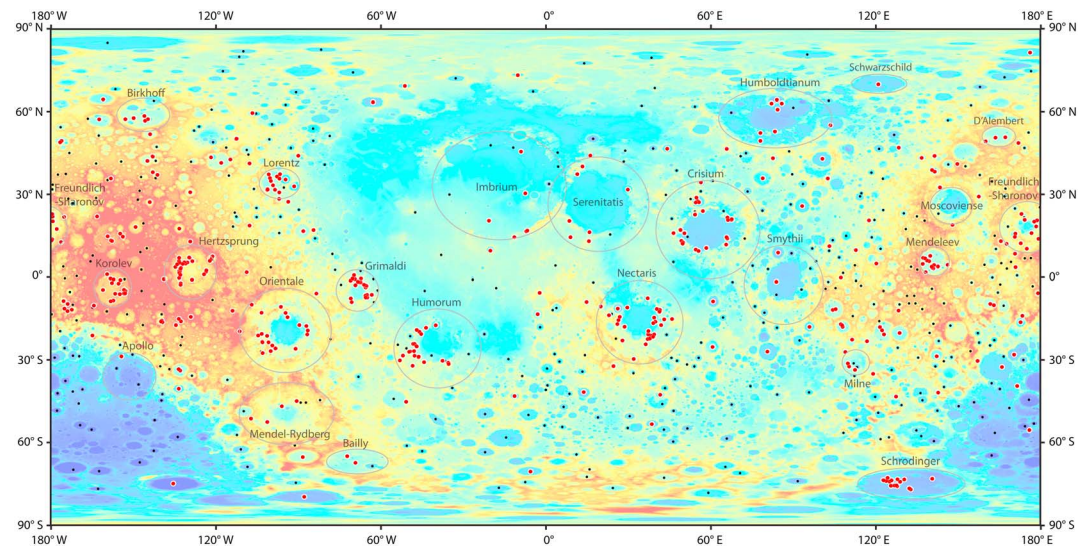


Figure 5. The red circles highlight the M^3 identifications of pure crystalline plagioclase as identified by high $1.25\ \mu\text{m}$ integrated band depth (1.25IBD) values and confirmed with M^3 spectra. The smaller, black circles identify investigated craters that did not contain pure crystalline plagioclase. The locations of the red and black circles are center latitudes and longitudes for each of the craters. Table 1 provides a more detailed description of the pure crystalline plagioclase exposures within individual named craters. The background image is the Lunar Orbiter Laser Altimeter (LOLA) topography [Smith et al., 2010] overlain on a Lunar Reconnaissance Orbiter Camera (LROC) Wide Angle Camera (WAC) albedo [Robinson et al., 2010] global mosaic.

Lunar Orbiter Laser Altimeter (LOLA) to determine selenolocation [Paige et al., 2009; Boardman et al., 2011; Smith et al., 2010]. For this analysis, M^3 data are georeferenced to the Diviner data by projecting it into a simple cylindrical projection using a datum based on the LOLA data. This process ensures that the areas determined to be spectrally pure plagioclase given their high 1.25IBD values in the NIR M^3 data can be used to estimate the average CF value for pure plagioclase areas within the TIR Diviner data. M^3 and Diviner have roughly the same spatial resolutions, $\sim 140\text{--}280\text{ m/pixel}$ for M^3 and $\sim 200\text{ m/pixel}$ for Diviner; thus, a pixel is sampling roughly the same area in both data sets. For this analysis, only Diviner data from the 50 km orbit were used to constrain the spatial resolution of the Diviner data to $\sim 200\text{ m/pixel}$.

4. Results

4.1. M^3 Near Infrared Results

In this global analysis of the M^3 data set, we have identified spectrally pure crystalline plagioclase in the walls and ejecta of simple craters and in the walls, floors, central peaks, and ejecta of complex craters, most in association with nearside and farside impact basins. In Figure 5, all areas identified as pure crystalline plagioclase are mapped across the lunar surface. Analyzed target areas, where pure plagioclase was not identified, are also indicated for comparison. Table 1 provides the central latitude and longitude for each named crater, in which pure crystalline plagioclase has been identified as well as a summary of where in the crater (e.g., wall versus central peak) pure plagioclase was identified. Table S1 in the supporting information provides the central latitude and longitude for every location (named and unnamed), where spectrally pure plagioclase was identified. The exposures of spectrally pure plagioclase are clearly associated with the inner and sometimes outer rings of larger impact basins like Orientale, Hertzprung, Humorum, Nectaris, and Crisium as well as limited exposures associated with Mendel-Rydberg, Imbrium, Humboldtianum, Serenitatis, Smythii, and South Pole-Aitken (SPA) basins. In Imbrium basin, pure plagioclase is observed in two isolated massifs surrounded by basalt, Mons Pico and an unnamed massif to the west of Archimedes, both proposed to be remnants of the inner ring of the basin [de Hon, 1979; Spudis, 1993]. Detailed analyses of the exposures along the Inner Rook Mountains of Orientale Basin and the inner ring of Schrödinger Basin as identified by M^3 are discussed by Cheek et al. [2013] and Kramer et al. [2013], respectively. Pure, crystalline plagioclase is also identified in the peak ring structures of Grimaldi, Korolev, Lorentz, Mendeleev, and Schrödinger. Other peak ring basins, such as Coulomb-Sarton, Moscoviense, Schwarzschild, D'Alembert, and Milne have limited

Table 1. Pure Crystalline Plagioclase Identifications in Named Lunar Craters^a

Name	Latitude	Longitude	Distance (km)	Degradation ^b	Tompkins and Pieters Class ^c	SELENE MI Class ^d	Central Peak/Floor/Wall/Rim/Ejecta
Aitken	−16.3640	173.0312	130.0	2	A, GNTA1, GNTA2		Central peak (CP)/W wall
Aitken A	−14.0000	173.7000	13.0				SE and NW walls
Alden C	−22.6733	111.6756	56.7	3			CP
Alexander	40.3000	13.5000	81.0				E rim
Alphonsus	−13.4128	−2.8399	113.9	3	A		CP
Alter	18.7462	−107.7877	63.9	3			CP
Amici N	−11.8000	−172.5000	39.0				CP
Amici P	−12.3000	−174.1000	31.0				N, SE, S, SW, and W walls
Amici R	−11.4000	−175.2000	34.0				E wall
Amici T	−9.7000	−174.0000	43.0				CP/NE rim
Amici U	−8.7008	−175.5000	95.9	4			CP
Anaxagoras	73.4001	−10.1144	50.1	1		A	CP/floor/NE ejecta
Anderson	15.8000	171.1000	109.0				NE and SE rim/NE ejecta
Anderson L	14.6000	170.9000	14.0				NE wall/NW ejecta
Atlas	46.7071	44.3273	87.1	3	GNTA1, AG	A	NE floor/N, NE, and SE walls
Babakin	−20.8000	123.3000	20.0				S wall
Bailly D	−65.2000	−72.2000	23.0				W wall
Bailly F	−67.5000	−69.2000	16.0				S wall
Beaumont	−18.0000	28.8000	53.0				SE floor
Beaumont D	−17.0000	26.2000	11.0				N, SE, S, and W walls
Belkovich	61.5742	90.1994	204.1	3			W rim
Benedict	4.4000	141.5000	14.0				E, SE, SW, and NW walls
Bergman	7.0000	137.5000	21.0				SE wall
Birkhoff	58.7000	−146.1000	345.0				S floor
Birkhoff K	57.4648	−144.7510	58.1	3			SE and S rims
Birkhoff R	57.5000	−153.0000	27.0				NE wall
Bohnenberger	−16.2000	40.0000	33.0				NE floor/SE wall /NE rim/SW ejecta
Bohnenberger F	−17.4000	42.1000	13.0				SE wall
Bohnenberger F	−14.7000	39.6000	10.0				N wall
Bridgman	43.3795	137.0228	84.5	2	A, GNTA1		CP/N wall
Bridgman E	44.1000	141.7000	29.0				NW wall
Buffon	−40.5887	−133.5390	100.0	3			CP/E and SW floor
Bunsen C	44.2000	−90.0000	18.0				N and S walls
Buys-Ballot	20.8000	174.5000	55.0				NW wall
Capella A	−7.6000	37.2000	13.0				S wall
Carnot	52.0443	−144.0215	126.3	2			CP
Carpenter	69.5173	−51.2215	60.6	1	A, GNTA1	B	Floor/E and W walls
Carver	−43.4513	127.6358	64.6	3			CP
Catalán U	−45.1000	−90.6000	20.0				E and SW walls
Chadwick	−52.7000	−101.3000	30.0				NE, SE, and S walls/unnamed crater to SW
Chebyshev	−33.9978	−133.0092	174.7	3			S floor/NE rim
Chebyshev V	−33.5000	−133.6000	23.0				N, S, and NW walls
Cleomedes	27.6052	55.4783	135.7	2			CP
Cleomedes A	28.9000	55.0000	12.0				S wall
Cleomedes B	27.2000	55.9000	11.0				SE wall
Cleomedes G	24.0000	57.3000	20.0				E rim
Colombo	−15.1661	46.0978	83.1	2			CP
Compton	55.3000	103.8000	162.0		A, GNTA1, GNTA2	B	Peak ring
Condorcet T	11.8000	65.8000	15.0				NW wall
Copernicus	9.5912	−20.0583	94.8	1	GNTA1, GNTA2, AT	B	N wall
Coriolis Y	3.6000	171.2000	31.0				NE wall
Crookes	−10.3000	−164.5000	49.0		GNTA1, GNTA1, AT	C	W ejecta
Cyrillus A	−13.8000	23.1000	17.0			B	SE wall
Cyrillus G	−15.6000	26.6000	8.0				E wall
D'Alembert	50.8000	163.9000	248.0				S and C floor/SE rim
D'Alembert G	50.9000	167.5000	18.0				E and W walls
Daedalus	−5.8202	179.3439	93.7	2	A	B	CP
Dalton	17.0704	−84.4968	59.9	3			CP/S rim
Damoiseau D	−6.4000	−63.3000	17.0				NW wall
De Gasparis G	−27.0000	−49.3000	6.0				Unnamed crater to SW

Table 1. (continued)

Name	Latitude	Longitude	Distance (km)	Degradation ^b	Tompkins and Pieters Class ^c	SELENE MI Class ^d	Central Peak/Floor/Wall/Rim/Ejecta
Debye	49.6000	−176.2000	142.0				SW floor
Drygalski	−79.8833	−87.8761	165.1	2			CP
Dufay B	8.5000	171.0000	20.0				S, SW, and NW walls
Einstein A	16.7004	−88.2000	50.8	2	A		CP/N, S, and W walls/S and W ejecta
Eratosthenes	14.5005	−11.3000	57.9	1	A, GNTA1, GNTA2, AGN		CP
Eudoxus	44.2478	16.3313	66.3	1	A, GNTA1, GNTA2	B	CP
Evershed E	35.9000	−158.3000	73.0				SE rim
Fabricius	−42.8034	41.7893	76.2	2	A, GNTA1, GNTA2		CP
Fabry	43.0460	100.8223	177.4	3			CP/N floor
Fermi	−19.3000	122.6000	183.0				NW floor
Fourier	−30.3000	−53.0000	51.0				SE wall
Fourier C	−28.5000	−51.9000	14.0				N, SE, and SW walls
Fowler	42.3000	−145.0000	146.0				NE, S, SW, and NW rims
Fracastorius A	−24.4000	36.5000	18.0				SW wall
Fracastorius B	−22.5000	37.2000	27.0				N and E walls
Fracastorius G	−21.2000	38.3000	16.0				NE wall
Fracastorius J	−20.8000	37.4000	12.0				W rim/unnamed crater to S
Fracastorius T	−19.8000	37.4000	14.0				N rim
Fryxwell	−21.3000	−101.4000	18.0				E and SE walls
Gassendi	−17.4920	−40.0050	112.0	3	GNTA1		CP
Gassendi E	−18.4000	−43.5000	8.0			A	W wall
Gauss	35.9351	79.1061	169.4	3			CP/C floor
Geminus	34.4550	56.5804	82.7	1			CP/W floor
Giordano Bruno	35.9000	102.8000	22.0			A	W and NW ejecta
Glaisher	13.2000	49.5000	15.0				N and W walls
Glaisher B	12.6000	50.1000	18.0				W wall/SW ejecta
Golitsyn J	−27.6000	−103.0000	20.0			A	NE, S, and SW walls
Grigg	12.9000	−129.4000	36.0				C floor
Grimaldi B	−2.9000	−69.2000	22.0				SW and NW walls
Grimaldi D	−3.7000	−65.5000	22.0				W rim
Grimaldi G	−7.4000	−64.9000	13.0				N wall
Grimaldi S	−6.4000	−65.0000	11.0				NE and SW walls
Grimaldi T	−7.7000	−70.9000	12.0				N wall
Haldane	−1.7000	84.1000	37.0				CP
Hausen	−65.5000	−88.4000	167.0				CP
Hayford	12.7000	−176.4000	27.0				NW wall
Hayford U	14.0000	179.9000	21.0				N and SW walls/unnamed crater to SE
Hayn	64.4935	84.2892	85.9	1	GNTA1, GNTA2	B	CP / SE ejecta
Henry V	14.7000	−153.9000	26.0				N wall / unnamed crater to N
Herschel	−5.7000	−2.1000	40.0				CP
Hertzprung V	5.2000	−133.3000	39.0				S and SW walls/NE rim
Hevelius J	0.7000	−69.7000	14.0				SE wall/unnamed crater to W
Hilbert	−18.0648	108.2477	173.0	3			CP
Hilbert W	−17.1000	107.6000	20.0				N wall
Humboldt	−27.0858	80.8167	205.5	3			CP
Ioffe	−14.4011	−129.2000	85.9	1			CP
Izsak	−23.3000	117.1000	30.0				N and NE floor
Jackson	22.0630	−163.3255	71.0	1	GNTA1, GNTA2, AGN	A	CP/floor/E and W walls
Joliot	25.8557	93.4412	169.1	3	A, GNTA1		CP
Joule	27.2515	−144.1205	97.0	3			S wall
Kant	−10.6000	20.1000	33.0			A	C floor/N wall
Keeler	−9.7016	161.9597	161.1	2	A, AT		CP/C floor/E rim
King	4.9152	120.4802	76.8	1	GNTA2, AGN	A	C floor
Klute	37.2000	−141.3000	75.0				SW wall
Klute W	38.2000	−143.0000	13.0				N wall
Kopff	−17.4000	−89.6000	41.0				NE floor
Korolev G	−6.0000	−153.3000	12.0				NE and S walls
Korolev L	−6.0000	−156.7000	30.0				S wall
Korolev M	−8.4639	−157.3533	56.1	3			CP/S wall/SW rim
Kovalevskaya	30.8652	−129.4032	114.9	1	A, GNTA1, GNTA2		CP/S and W walls/W ejecta

Table 1. (continued)

Name	Latitude	Longitude	Distance (km)	Degradation ^b	Tompkins and Pieters Class ^c	SELENE MI Class ^d	Central Peak/Floor/Wall/Rim/Ejecta
Kurchatov	38.4012	141.7837	117.2	3			floor
Lacchini	41.3838	−107.8028	58.0	1			CP/S wall/S rim/S and SW ejecta
Landau	41.6000	−118.1000	214.0				SE and C floor/E rim
Langrenus	−8.7830	61.0639	130.8	1	GNTA1, AN, T		CP
Laue	28.4566	−96.9788	88.6	2			NE rim/unnamed crater to N
Leibnitz S	−39.6000	171.8000	28.0			A	Unnamed crater to NE
Leonov	19.0000	148.2000	33.0				S wall
Leuschner	1.8000	−108.8000	49.0		A, GNTA1		CP
Liebig	−24.3000	−48.2000	37.0				N wall/S rim/S and SE ejecta
Liebig A	−24.3000	−47.7000	12.0				N, NE, and S walls/SW rim
Liebig B	−25.0000	−47.1000	9.0				S wall
Lindenau	−32.3901	24.7483	52.3	2	A, GNTA1, GNTA2		CP
Lobachevskiy	9.7837	113.0781	89.5	1	GNTA1, GNTA2		CP
Lohrmann	−0.5000	−67.2000	30.0				C floor/S ejecta,
Lohrmann B	−0.7000	−69.4000	14.0				E and S walls
Lohrmann E	−1.7000	−67.4000	10.0				SE rim
Lohrmann N	−0.6000	−70.1000	8.0				NW wall
Lorentz P	31.8000	−98.5000	38.0				N rim/unnamed crater to W
Lorentz R	33.4000	−99.2000	33.0				E and NE rims
Lorentz U	35.0000	−100.0000	22.0				S and SW walls/unnamed crater to N
Lowell	−12.9460	−103.3877	65.9	1	GNTA1, GNTA2, AG	C	SE rim
Lowell W	−10.0000	−107.0000	18.0				S rim
Mach	18.2105	−149.2718	180.1	3	A	B	CP
Mädler	−11.0000	29.8000	27.0				SE wall
Manilius	14.5000	9.1000	38.0			A	N, NE, and NW walls
Maunder	−14.5356	−93.9164	55.7	1	GNTA1, GNTA2, AG		N and NW walls/NW ejecta
Maurolycus	−41.8517	13.9445	112.7	3	A		floor/N rim
Mendel J	−51.5116	−107.2637	57.9	1			CP
Menelaus	16.3000	16.0000	26.0				NE and E walls
Mercurius	46.6547	66.0265	66.6	2			CP
Mersenius C	−19.8000	−45.9000	14.0				N and NW walls
Mersenius S	−19.2000	−46.9000	16.0				N wall
Michelson	6.6258	−121.6085	123.0	3			SW floor
Michelson W	7.5000	−121.3000	25.0				S wall
Milne	−31.4000	112.2000	272.0				Floor
Milne L	−33.7000	112.7000	26.0				NE and NW walls
Moiseev Z	11.2000	103.4000	80.0				SE wall
Moissan	4.8000	137.4000	21.0				N and NE walls
Mons Pico	45.7000	−8.9000					NE, S, NW, and C
Moore F	37.4000	−175.0000	24.0				N ejecta
Moretus	−70.6584	−5.4423	115.6	1			CP
Morse	21.8759	−175.2973	76.9	2	A, GNTA1		CP
Morse T	22.0000	−179.5000	34.0				E rim
Necho	−5.0000	123.1000	30.0			C	Floor
Neper	8.8506	84.7214	147.7	2	A, GNTA1, GNTA2		CP
Nernst	35.5190	−94.6737	123.0	2			CP/N, SE, S, and NW walls/SE ejecta/unnamed crater to N
Nernst T	35.8000	−96.9000	25.0				S wall
O'Day	−30.4780	157.3639	62.2	1	A, GNTA1, GNTA2	A	CP
Olcott	20.6146	117.8421	80.2	1	A, GNTA1, GNTA2		CP
Palmieri	−28.6000	−47.7000	40.0				SE rim/unnamed crater to SE
Palmieri A	−32.2000	−48.4000	21.0				S wall
Paschen L	−16.4000	−139.5000	38.0				N, NW, and W rims
Paschen M	−16.1000	−140.0000	94.0				Floor
Pasteur G	−11.6000	105.7000	21.0				NW rim/unnamed crater to N
Pavlov	−28.8000	142.5000	148.0				NW floor
Petavius	−25.3914	60.8401	180.0	2		A	CP
Piccolomini	−29.7288	32.1532	84.5	2	A, GNTA1	B	CP
Pizzetti	−35.1362	119.2907	53.9	3			CP
Plante	−10.2000	163.3000	37.0				NW wall/N rim

Table 1. (continued)

Name	Latitude	Longitude	Distance (km)	Degradation ^b	Tompkins and Pieters Class ^c	SELENE MI Class ^d	Central Peak/Floor/Wall/Rim/Ejecta
Plaskett	81.6630	176.5005	109.0	2			CP
Polybius A	−23.0000	28.0000	17.0				SE wall
Posidonius	31.8626	29.9959	99.0	3	A		CP/SE and SW rims
Poynting	17.6338	−133.3849	128.1	2			CP/SW floor
Proclus	16.1000	46.8000	28.0			A	N wall
Pythagoras	63.6217	−62.8328	128.7	1	A, GNTA1	A	CP
Pytheas	20.5000	−20.6000	20.0				NW wall/N rim
Raimond	14.8142	−159.4866	63.5	3			N and S floor/N, NE, and S walls/NE rim
Raimond K	13.3000	−158.2000	34.0				CP/N, E, and S walls/NE rim/NE ejecta
Riccioli G	−1.3000	−71.0000	15.0				NE, E, SW, W, and NW walls
Richards	7.7000	140.1000	16.0				N, E, SE, and S walls/NE rim
Rontgren	33.0563	−91.5315	123.2	3			NW rim
Rowland	57.4000	−162.5000	171.0				Floor
Rydberg	−46.5000	−96.3000	49.0			A	NW wall
Ryder	−44.5000	143.2000	17.0			A	NW wall/SE rim/NE and W ejecta
Saha E	−0.2000	107.6000	28.0				N and NE walls
Santbech N	−20.8000	39.6000	13.0				SW wall
Scaliger	−27.2108	109.1783	85.0	1	A, GNTA1, GNTA2, AG		E, SW, and W floor/NE and E walls
Schluter	−5.9146	−83.4496	85.5	2			CP/unnamed crater to SE
Schuster	4.4618	146.4325	103.3	3			CP
Schwarzschild	70.1000	121.2000	212.0				Peak ring
Sharnov	12.2766	173.0517	78.7	1	A, GNTA1, GNTA2	B	NW wall/unnamed craters to E, SE, and NW
Shirakatsi	−12.1003	128.6000	50.8	2			CP
Sklodowska	−18.0415	96.1224	125.7	2			CP
Slipher	49.4362	160.3040	76.0	2	A, GNTA1		E wall
Sommerfeld	64.5790	−161.0714	139.2	2			Floor
South Ray	−9.2000	15.4000	1.0			A	SE and NW ejecta
Spencer Jones	13.0691	165.8195	88.9	2			CP/floor
Spencer Jones H	12.1000	167.9000	17.0				NE wall
Steno Q	29.3000	157.8000	29.0				W and NW rims
Stromgren X	−17.4000	−134.6000	42.0				CP/floor/SW wall/E and SE rim
Sulpicius Gallus M	20.4000	8.7000	5.0				E ejecta
Theophilus	−11.3957	26.3292	98.0	1	A, GNTA1, GNTA2, AT		CP
Thomson	−32.7000	166.2000	117.0				NW rim
Tsiolkovsky	−20.2614	128.9814	185.1	1	A, GNTA1, GNTA2, AT	A	CP/E and SE walls/SW rim
Tycho	−43.2703	−11.2856	81.6	1	GNTA2, AG, AGN, G	A	SE wall/SE rim
Van de Graff	−28.1884	170.6549	146.3	3			CP
Vavilov	−0.6941	−138.9447	97.9	1	A, GNTA1, GNTA2, AGN	A	CP/NE floor/N wall
Virtanen	15.5000	176.7000	44.0			A	CP/floor/N, NE, SE, S, SW walls
Vitello	−30.4000	−37.5000	42.0		GNTA1, GNTA2		CP/floor
Vitello B	−31.1000	−35.4000	11.0				SE wall
Vitello L	−31.6000	−35.3000	7.0				N wall
Vlacq	−53.4751	38.7340	87.2	2	A		CP
Wiener F	41.2000	150.0000	47.0				Floor
Wood	43.6262	−121.7809	81.0	3			CP
Yerkes E	15.9000	50.6000	10.0				S and SE walls
Zeeman	−75.0430	−135.5966	185.2	3			CP
Zsigmondy S	59.7000	−106.7000	64.0				W wall

^aCrater central latitudes and longitudes as well as crater diameters were taken from the complex crater survey of *Head et al.* [2010] and *Baker et al.* [2012], and when those were not available crater central latitudes and longitudes were taken from the U.S. Geological Survey [Anderson and Whitaker, 1982; Blue, 2004].

^b*Baker et al.* [2012] describes the degradation class of the central peak where 1 = freshest and 4 = most degraded.

^c*Tompkins and Pieters* [1999].

^d*Ohtake et al.* [2009].

identifications of pure plagioclase in their peak rings. However, pure regions of crystalline plagioclase were not identified in three peak ring basins within SPA basin, Planck, Poincare, and Apollo (with the exception of one small exposure on northern rim). Additionally, it should be noted that aside from Schrödinger basin, the interior of SPA has a limited number of detections of pure crystalline plagioclase. Observations in the interior

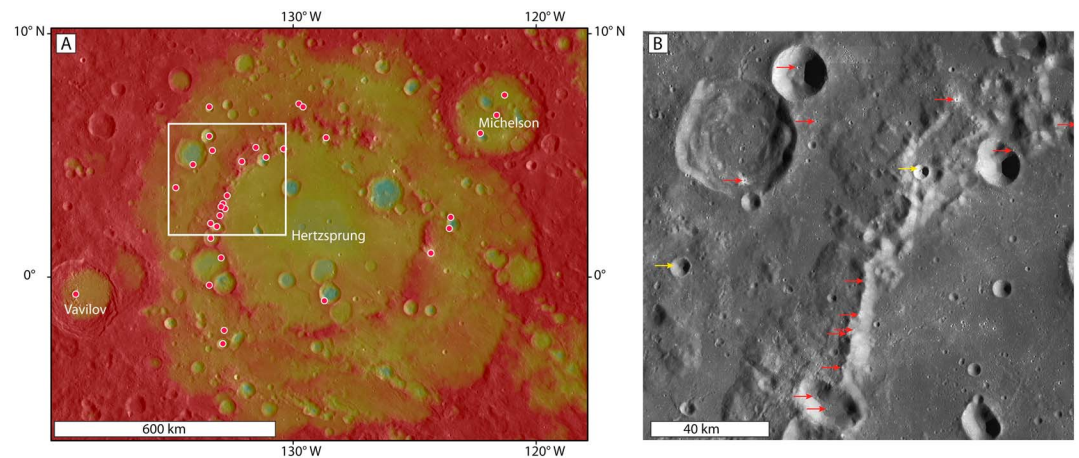


Figure 6. (a) Hertzprung basin (2°N , 128°W), a 570 diameter basin of Nectarian age on the lunar farside [Spudis, 1993]. The red circles indicate the identifications of pure crystalline plagioclase. The background image is the LOLA topography overlay on a LROC WAC mosaic. (b) LROC WAC mosaic of the northwest inner ring of Hertzprung basin. The red arrows indicate the exposures of pure crystalline plagioclase in small, fresh craters (<1 km in diameter). The yellow arrows indicate the exposures in the walls of larger, fresh craters (4–7 km in diameter). Plagioclase exposures in Hertzprung basin are dominated by small, fresh craters on the inner ring as well as small, fresh craters in the walls and rims of other craters. The white box highlights the region examined in Figure 6b.

of the basin include the southeastern rim of Hess crater, the central peak of Zeeman, and the northwestern wall of Leibnitz S.

Examples of the types of exposures of spectrally pure, crystalline plagioclase observed in and around basins are highlighted in Figures 6 and 7. Exposures of pure crystalline plagioclase in the inner rings of many of the lunar basins are dominated by smaller, fresh craters and blocky units exposed on massifs forming the rings as well as small fresh crater exposures on the basin floors. Pure crystalline plagioclase exposures in the inner ring of Hertzprung basin (2°N , 128°W), a 570 km Nectarian-aged basin on the lunar farside, are dominated by

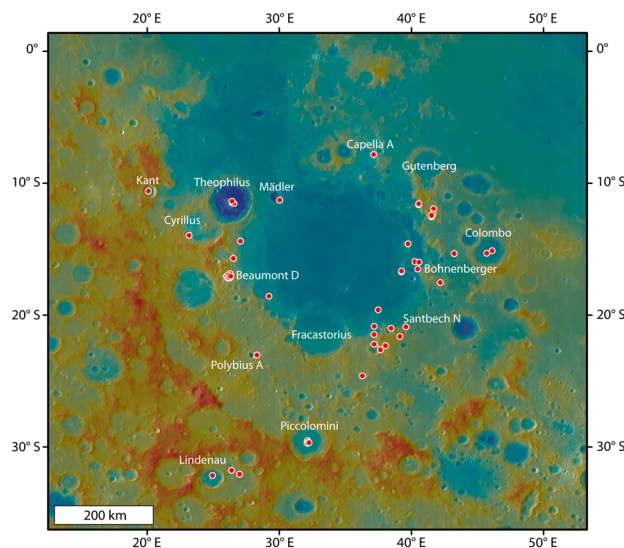


Figure 7. Nectaris basin (16°S , 34°E), a 400 km inner ring diameter basin on the lunar nearside of Nectarian age [Spudis, 1993]. The red circles indicate the regions identified as pure crystalline plagioclase in the innermost mare-bounding ring, an intermediate ring 620 km in diameter, and the main rim of the basin [Spudis, 1993]. The background image is the LOLA topography overlay on the LROC WAC mosaic.

small (<7 km in diameter), fresh craters as seen in Figure 6. While Michelson and Vavilov craters have exposed pure crystalline plagioclase on the rim of the basin, most of the exposures are observed in the northwestern portion of the inner ring. Lunar Reconnaissance Orbiter Camera (LROC) Wide Angle Camera (WAC) imagery for that portion of the ring in Figure 6b shows that two types of exposures are observed. First, the red arrows highlight small, fresh craters (<1 km in diameter) exposing pure plagioclase in the floor, walls, and rims of craters as well as in the massifs forming the ring structure. The freshness or immaturity of the craters is indicated by the high-albedo nature of their ejecta compared to the albedo of the surrounding materials. The yellow arrows highlight the walls of larger, fresher craters (4–7 km in diameter), where pure plagioclase exposures are observed. Similar types of pure crystalline

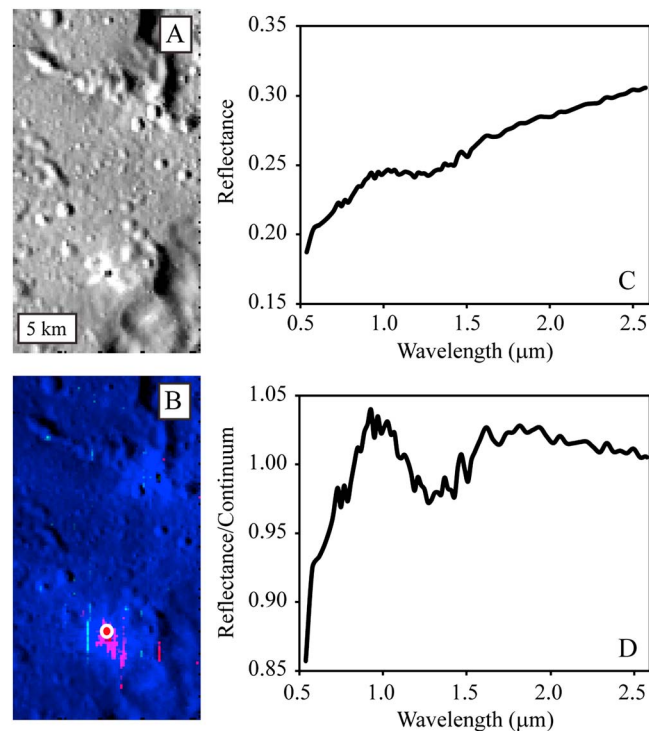


Figure 8. (a) M^3 spectral band 84 radiance including North Ray (8.8°S, 15.5°E) and South Ray (9.2°S, 15.4°E) craters. (b) Spectral parameter map of the same region, where red = 1.25 μ m IBD, green = 1.00 μ m IBD, and blue = 1.58 μ m IBD. The areas of pure crystalline plagioclase are red/pink in color. (c) M^3 reflectance spectrum of the high 1.25 μ m IBD value region in the northwest ejecta blanket of South Ray as marked by the red circle in Figure 8b. (d) M^3 reflectance spectrum divided by a continuum to highlight the 1.25 μ m absorption band diagnostic of crystalline plagioclase.

plagioclase exposures dominate the peak rings of Grimaldi, Korolev, and Mendelev basins.

In many of the multiring basins, the exposures of spectrally pure plagioclase are observed in multiple rings of each basin. In Nectaris basin, a multiring basin on the lunar nearside (16°S, 34°E), pure crystalline plagioclase is observed in the 400 km diameter innermost mare-bounding ring, an intermediate ring 620 km in diameter, and the main rim of the basin. Definitions of rings and their diameters are taken from *Spudis* [1993]. As seen in Figure 7, most of the pure crystalline plagioclase identifications are observed in the innermost mare-bounding ring. Inner ring exposures include the central peak of Theophilus and southeast wall of Bohnenberger crater as well as the walls and ejecta of simple craters: Beaumont D, Bohnenberger E, Bohnenberger F, Capella A, Santbech N, and multiple satellite craters of Fracastorius. Other identifications of pure crystalline plagioclase in the mare-bounding ring include small (<4 km in diameter), fresh craters including several identifications south of Gutenberg crater. The observations of

pure crystalline plagioclase in the 620 km intermediate ring include the central peak of Colombo and the walls of Cyrillus A and Polybius A. The exposures of pure crystalline plagioclase on the main rim are observed in the central peak of Piccolomini and a small crater exposure on the floor of Kant. Similar types of pure crystalline plagioclase exposures are observed in other multiring basins, including Humorum, Crisium, and Serenitatis basins as well as the peak ring of Freundlich-Sharonov basin.

Examples of the types of exposures of spectrally pure crystalline plagioclase observed in a range of simple to complex craters in the M^3 data set are presented in Figures 8–11. In Figure 8, we examine South Ray crater (9.2°S, 15.4°E), a simple crater 680 m in diameter located in the Decartes Mountain formation to the west of Mare Nectaris. Samples thought to be derived from South Ray crater were collected and returned by the Apollo 16 astronauts. The exposures of spectrally pure plagioclase were first identified in the ejecta of South Ray crater by *Ohtake et al.* [2009]. The M^3 spectral parameter map in Figure 8b highlights the spectrally pure plagioclase units in the northwestern and southeastern portions of South Ray's ejecta blanket. M^3 reflectance and continuum-removed spectra in Figures 8c and 8d highlight the 1.25 μ m absorption diagnostic of crystalline plagioclase. The lack of absorptions at 1 and 2 μ m indicate that this portion of the northwestern ejecta exhibits pure crystalline plagioclase ($\geq 99\%$ plagioclase).

Jackson crater (22.063°N, 163.3255°W) is a complex crater 71.0 km in diameter on the northwestern rim of Dirichlet-Jackson basin, an ancient basin located on the lunar farside. Pure plagioclase was first discovered in Jackson crater by *Ohtake et al.* [2009]. In Figure 9b, pure plagioclase is shown to occur in the western and eastern walls, the floor, and the central peak structure of Jackson crater as indicated by pixels with high 1.25IBD values. As seen in Figure 9c, pure plagioclase is abundant in the entire central peak structure, in particular the steep slopes of the main central uplift. Pyroxene-rich units are also observed on the top or capping unit of the main central uplift as indicated by pixels with high 1.00IBD values in Figure 9c. M^3

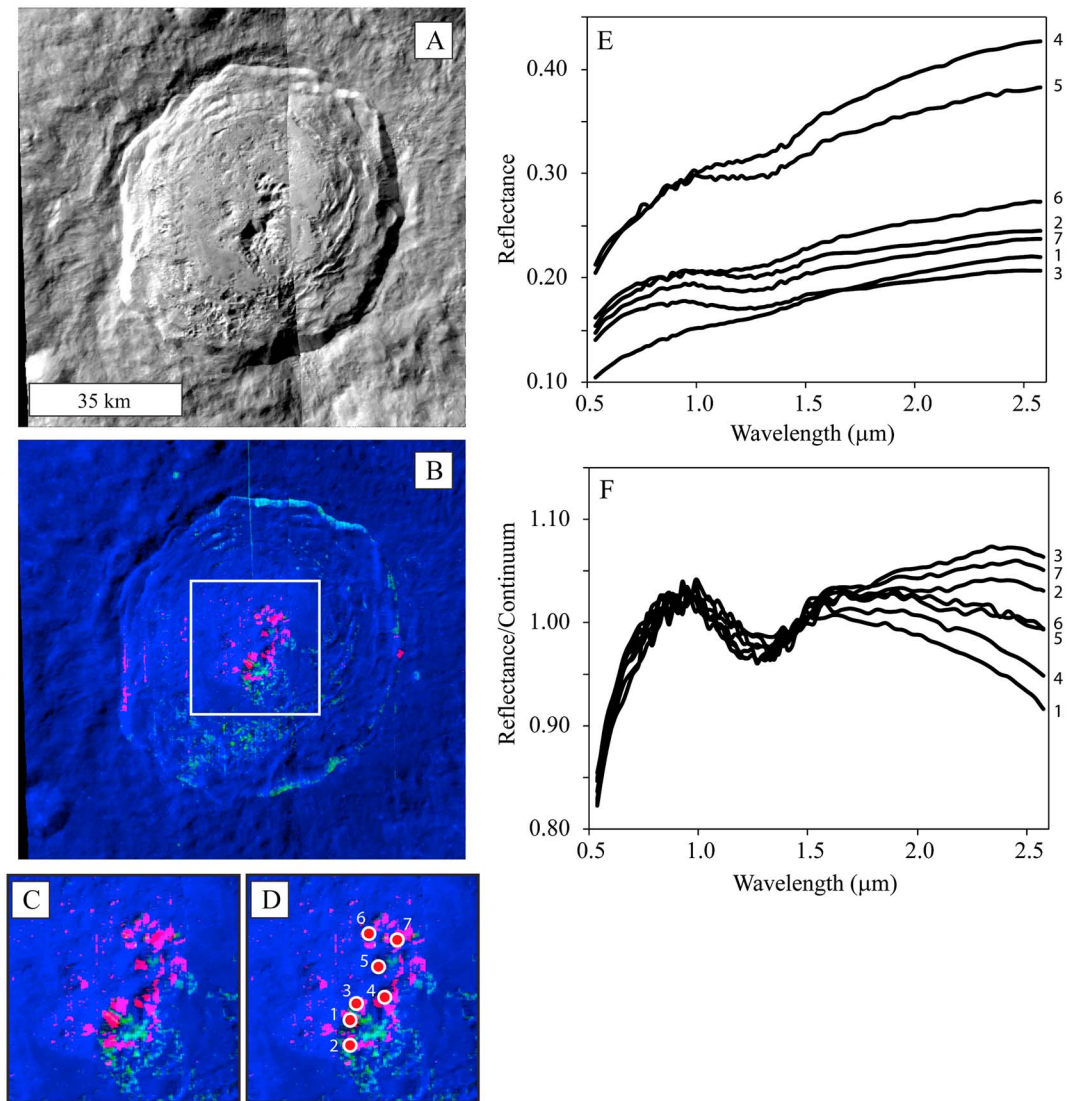


Figure 9. (a) M^3 spectral band 84 radiance of Jackson crater (22.063°N, 163.3255°W). (b) Spectral parameter map of the same region, where red = 1.25 μ m IBD, green = 1.00 μ m IBD, and blue = 1.58 reflectance. The areas of pure crystalline plagioclase are red/pink in color. (c) Spectral parameter map of the central peak structure of Jackson crater. (d) Spectral parameter map with red circles highlighting 5 \times 5 pixel regions where spectra were extracted. (e) M^3 reflectance spectra of the high 1.25 μ m IBD value regions in the central peak structure of Jackson as marked by the red circles in Figure 9d. (f) M^3 reflectance spectra divided by continua to highlight the 1.25 μ m absorption band diagnostic of crystalline plagioclase. The white box highlights the region examined in Figures 9c and 9d.

reflectance and continuum-removed spectra were extracted from the central peak as designated in Figure 9d and are shown in Figures 9e and 9f. These spectra highlight examples of the 1.25 μ m absorption diagnostic of crystalline plagioclase observed in the central peak structure of Jackson crater. The lack of absorptions at 1 and 2 μ m indicate that crystalline plagioclase is not only abundant in the central peak but is also clearly spectrally pure.

Humboldt crater (27.0858°S, 80.167°E), a complex crater 205.5 km in diameter on the southeastern edge of the pre-Nectarian-aged Balmer-Kapteyn basin, is examined in Figure 10. As seen in Figure 10a, the central peak of Humboldt is a good example of a central peak structure transitioning between a singular, central uplift to a central ring structure. The floor of Humboldt crater has radial and concentric fractures and dark mantling deposits along the northeastern, northwestern, and southwestern walls. The central peak structure, including the central uplift and the northern ridge portions, is dominated by spectrally pure plagioclase (Figures 10b and 10c). M^3 reflectance and continuum-removed spectra (Figures 10e and 10f) extracted from

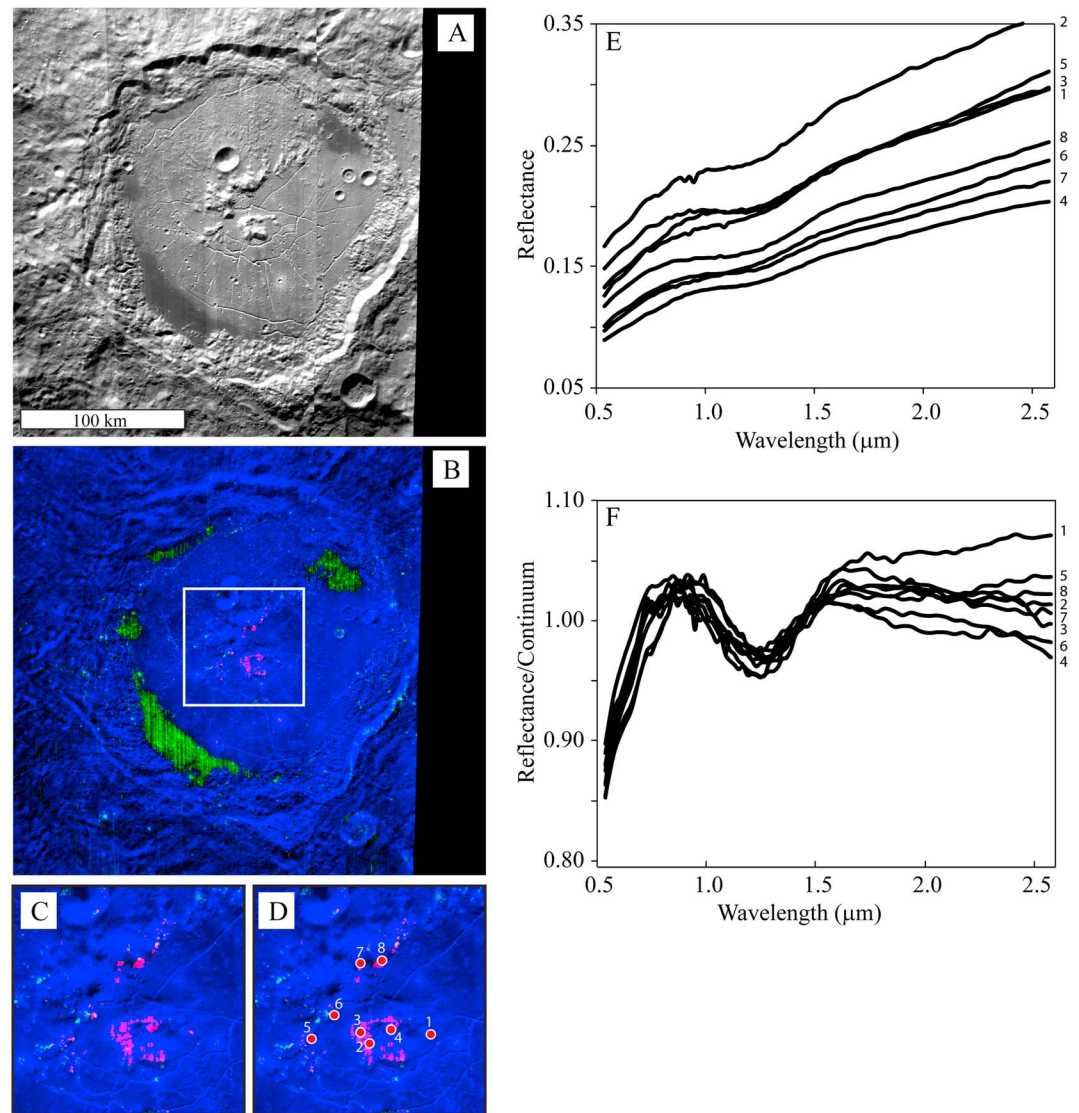


Figure 10. (a) M^3 spectral band 84 radiance of Humboldt crater (27.0858°S, 80.167°E). (b) Spectral parameter map of the same region, where red = 1.25 μ m IBD, green = 1.00 μ m IBD, and blue = 1.58 reflectance. The areas of pure crystalline plagioclase are red/pink in color. (c) Spectral parameter map of the central peak structure of Humboldt crater. (d) Spectral parameter map with red circles highlighting 5 \times 5 pixel regions where spectra were extracted. (e) M^3 reflectance spectra of the high 1.25 μ m IBD value regions in the central peak structure of Humboldt as marked by the red circles in Figure 10d. (f) M^3 reflectance spectra divided by continua to highlight the 1.25 μ m absorption band diagnostic of crystalline plagioclase. The white box highlights the region examined in Figures 10c and 10d.

the central peak as designated in Figure 10d highlight the range of 1.25 μ m diagnostic absorptions observed in Humboldt's central peak. Again, the lack of absorptions at 1 and 2 μ m indicate that the portions of the central peak structure are pure crystalline plagioclase.

In the Jackson and Humboldt crater examples, an abundance of pure crystalline plagioclase is observed in their central peak structures; however, these types of observations are rare. Typically, the exposures of pure crystalline plagioclase are small and isolated as seen in the central peaks of Keeler and Aitken craters in Figure 11. Keeler crater (9.7016°S, 161.9597°E) (Figures 11a and 11b, first column) is a complex crater 161.1 km in diameter located in the center of the pre-Nectarian-aged Keeler-Heaviside basin. Aitken crater (16.3640°S, 173.0312°E) (Figures 11a and 11b, second column) is a complex crater 130.0 km in diameter located on the northern rim of SPA. Isolated portions of each of their central peaks are identified as crystalline plagioclase in Figure 11c. M^3 reflectance and continuum-removed spectra extracted from the central peaks highlight the

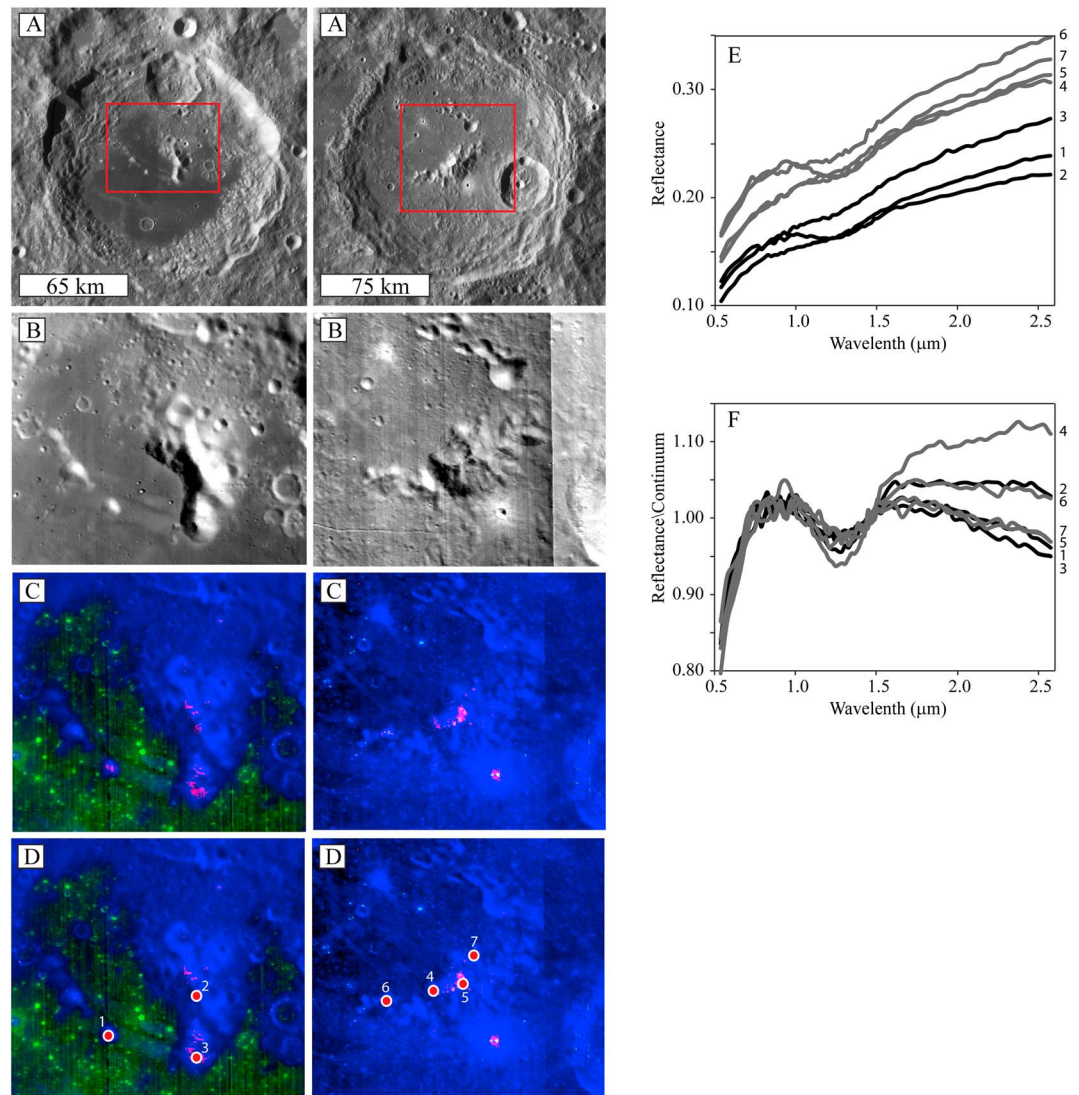


Figure 11. Central peaks of (first column) Aitken (16.3640°S, 173.0312°E) and (second column) Keeler (9.7016°S, 161.9597°E) craters. (a) LROC WAC albedo images. (b) M^3 spectral band 84 radiance. (c) Spectral parameter map of the same region, where red = 1.25 μ m IBD, green = 1.00 μ m IBD, and blue = 1.58 reflectance. The areas of pure crystalline plagioclase are red/pink in color. (d) Spectral parameter map with red circles highlighting 5×5 pixel regions where spectra were extracted. (e) M^3 reflectance spectra of the high 1.25 μ m IBD value regions as marked by the red circles in Figure 11d. (f) M^3 reflectance spectra divided by continua to highlight the 1.25 μ m absorption band diagnostic of crystalline plagioclase. The red boxes highlight the regions examined in Figures 11c and 11d.

1.25 μ m absorption diagnostic of crystalline plagioclase and the lack of absorptions at 1 and 2 μ m indicating that the portions of the central peak structure of each crater are pure crystalline plagioclase.

Although most of the regions identified as having spectrally pure plagioclase show no other diagnostic absorption bands due to mafic minerals within the same crater, there are some cases where units of distinct mafic minerals are associated with the units of pure plagioclase. A good example is seen in the walls of Proclus crater in Figure 12. Proclus crater (16.10°N, 46.8°E) is a 28.0 km simple crater located on the northwestern rim of Crisium basin. In Figure 12b, the M^3 spectral map highlights units rich in pure crystalline plagioclase with separate isolated exposures of pyroxene and olivine. M^3 reflectance spectra that were extracted from crystalline plagioclase-, pyroxene-, and olivine-rich wall units are designated in Figure 12c and displayed along with continuum-removed spectra in Figures 12d and 12e. In some cases, pure plagioclase units are adjacent to mafic units as seen in the plagioclase and pyroxene units in the northern wall of Proclus

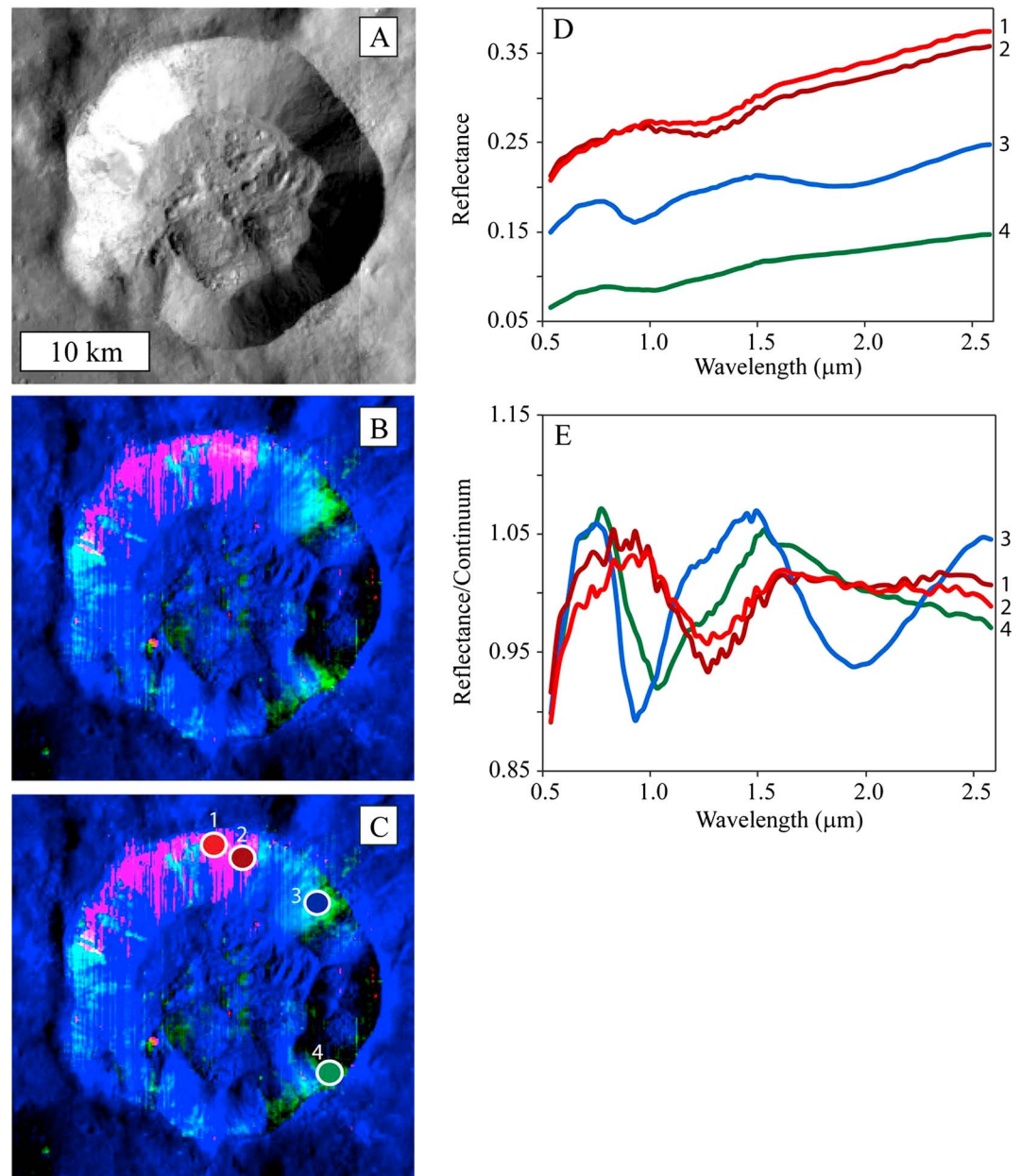


Figure 12. (a) M^3 spectral band 84 radiance of Proclus crater (16.10°N, 46.8°E), a 28.0 km crater on the northwestern rim of Crisium basin. (b) Spectral parameter map of the same region, where red = 1.25 μ m IBD, green = 1.00 μ m IBD, and blue = 1.58 reflectance. The areas rich in crystalline plagioclase are red/pink in color, and the areas rich in mafic minerals are green and cyan. (c) Spectral parameter map with colored circles highlighting 5 \times 5 pixel regions where spectra were extracted. (d) M^3 reflectance spectra of regions rich in plagioclase (red spectra and dots), pyroxene (blue spectrum and dot), and olivine (green spectrum and dot) (Figure 12c). (e) M^3 reflectance spectra divided by continua to highlight the diagnostic absorption bands of Fe-bearing minerals.

crater. In other cases, pure plagioclase is separated from mafic units as seen in the plagioclase and olivine-rich regions in the northern and southern walls of Proclus in Figure 12b.

While the main focus of this global analysis is on the exposures of pure anorthosite ($\geq 99\%$ plagioclase), areas of nonpure anorthosite are also identified and are characterized by spectra with multiple features owing to a diagnostic absorption near 1.25 μ m from plagioclase and a weak to subequal diagnostic absorption near 1 μ m from pyroxene (a “w” shape spectrum). The nonpure anorthosite spectra likely correspond to the exposures containing ~ 96 – 98 vol % plagioclase by comparisons with the mixing models of Cheek *et al.* [2013].

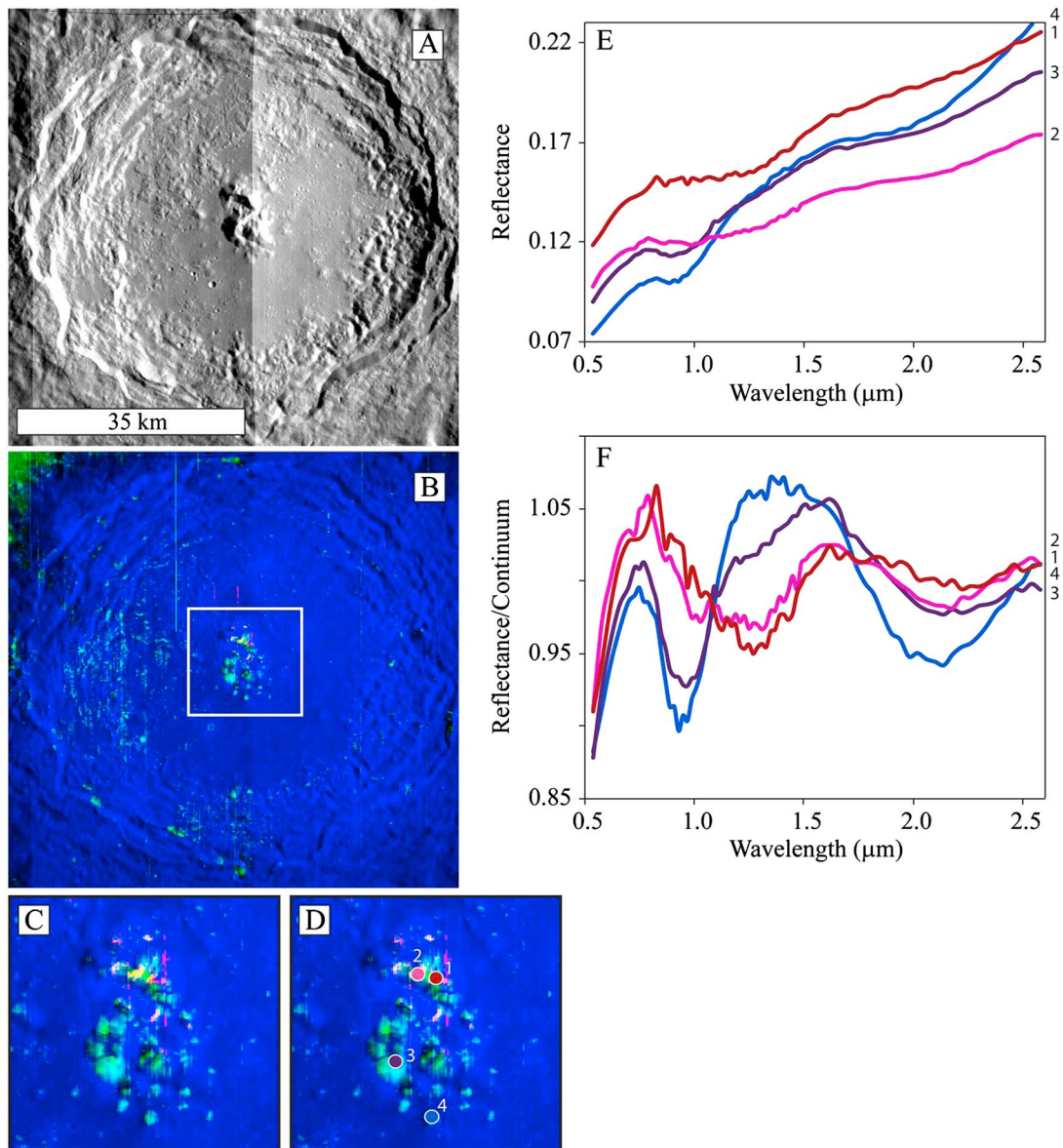


Figure 13. (a) M^3 spectral band 84 radiance of Langrenus crater (8.783°S, 61.0639°E), a 130.8 km crater located between Nectaris and Smythii basins. (b) Spectral parameter map of the same region, where red = 1.25 μ m IBD, green = 1.00 μ m IBD, and blue = 1.58 reflectance. The areas of pure crystalline plagioclase (pure anorthosite) are red/pink in color, and the areas rich in mafic minerals are green and cyan. The areas of nonpure anorthosite ($\leq 98\%$ plagioclase) are indicated by cyan-yellow-orange pixels. (c) Spectral parameter map of the central peak structure of Langrenus crater. (d) Spectral parameter map with colored circles highlighting 5×5 pixel regions where spectra were extracted. (e) M^3 reflectance spectra of regions rich in plagioclase (red spectra and dots), pyroxene (blue spectrum and dot), and mixtures of plagioclase and pyroxene (purple and pink spectra and dots) (Figure 13d). (f) M^3 reflectance spectra divided by continua to highlight the diagnostic absorption bands of Fe-bearing minerals. The white box highlights the region examined in Figures 13c and 13d.

Previous studies using M^3 data have shown in detail how the purity of anorthosite can vary across the Inner and Outer Rook Mountains of Orientale [Cheek *et al.*, 2013], the inner ring of Schrodinger basin [Kramer *et al.*, 2013], and the central peak of Tsiolkovsky crater [Cheek and Pieters, 2012] by identifying spectrally distinct units of pure and nonpure anorthosite. Figure 13 highlights the central peak of Langrenus crater (8.783°S, 61.0639°E), a 130.8 km complex crater located in between Nectaris, Crisium, and Smythii basins. Langrenus is a region newly identified as containing distinct units of pure anorthosite along with nonpure anorthosite and mafic units in the central peak of the crater. Units spectrally dominated by pure anorthosite, nonpure anorthosite, and mafic lithologies are highlighted in the M^3 spectral maps in Figure 13. M^3 reflectance and continuum-removed spectra in Figures 13e and 13f highlight example spectra for each compositional unit

Table 2. Pure Plagioclase Regions Analyzed With Diviner TIR Data

Crater	Central Peak/Floor/Wall/Ejecta	Median CF	Average CF	SD
Aitken	CP	7.95	7.93	0.08
Alphonsus	CP	7.94	7.93	0.02
Beaumont D	SW wall	7.92	7.90	0.12
Buy's-Ballot	N wall	7.95	7.94	0.03
Cleomedes A	S wall	7.93	7.93	0.02
Cleomedes B	S wall	7.93	7.90	0.08
Colombo	CP	8.03	8.03	0.01
Einstein A	CP	8.01	8.01	0.01
Fabricius	CP	7.92	7.92	0.04
Geminus	CP	7.88	7.87	0.05
Hercules	N wall of crater in Hercules floor	7.93	7.92	0.02
Humboldt	CP	7.90	7.89	0.05
Jackson	CP	7.88	7.87	0.05
Joliot	CP	7.94	7.94	0.01
Kant	Small crater in floor	7.91	7.89	0.04
Keeler	CP	7.93	7.92	0.03
Kovalevskaya	CP	7.94	7.91	0.08
Langrenus	CP	7.95	7.94	0.02
Menelaus	S wall	7.94	7.93	0.05
Mercurius	CP	7.99	7.99	0.02
O'Day	CP	7.95	7.93	0.04
Olcott	CP	7.94	7.94	0.04
Petavius	CP	7.94	7.92	0.07
Piccolomini	CP	7.99	7.98	0.02
Poynting	CP	7.98	7.97	0.03
Proclus	N wall	7.93	7.92	0.02
Ryder	N, W, and S walls	7.93	7.92	0.04
Schluter	CP	7.95	7.93	0.05
South Ray	NE and SW ejecta	8.01	8.00	0.02
Theophilus	CP	7.95	7.95	0.02
Tsiolkovskiy	CP	7.93	7.91	0.06
Van de Graff	CP	7.95	7.95	0.03
Vavilov	CP	7.97	7.96	0.03
Virtanen	CP / N, NE and E walls	7.91	7.90	0.03
Vlacq	CP	7.93	7.92	0.04
Wiener F	N floor	7.96	7.95	0.04
Wood	CP	7.97	7.96	0.04

observed. Examples of nonpure anorthosite spectra include spectra 2 and 3 in Figures 13e and 13f, where perceptible 1, 1.25, and 2 μm absorption bands are observed in both spectra indicating the presence of plagioclase and pyroxene. As the abundance of pyroxene increases within anorthosite, the strength of the 1 and 2 μm absorption bands increases, and the spectrum becomes more pyroxene like as seen in spectrum 3 in Figures 13e and 13f. Spectrum 3 is still considered a nonpure anorthosite as it has a discernible 1.25 μm absorption band likely due to plagioclase. However, it should be noted that the absorption near 1.25 μm cannot be uniquely identified from the 1.2 μm absorption band in pyroxene spectra owing to Fe^{2+} in the M1 crystallographic site [Klima *et al.*, 2008] (Figure 1). Cheek *et al.* [2013] classified units with similar spectral shapes as Class C, which are estimated to contain ≤ 95 vol % plagioclase.

4.2. Diviner Thermal Infrared Results

In this part of the analysis, Diviner thermal infrared data for 37 highland craters that have good coverage over large exposures of spectrally pure plagioclase regions are examined. Table 2 provides a list of the highland craters examined in this work, the analyzed portion of each crater, as well as the median, mean, and standard deviation of the Diviner CF values. Examples of the Diviner analysis for spectrally pure crystalline plagioclase exposures in South Ray's ejecta blanket as well as the central peaks of Jackson and Humboldt craters are shown in Figures 14–16. In Figure 14, we examine the units identified in M^3 data as spectrally pure plagioclase in the northwestern and southeastern portions of South Ray crater's ejecta blanket. A Diviner CF map for the same region (Figure 14c) shows a similar distribution of units having CF values ($7.5 \leq \text{CF value} \leq 8.0 \mu\text{m}$) consistent with the presence of

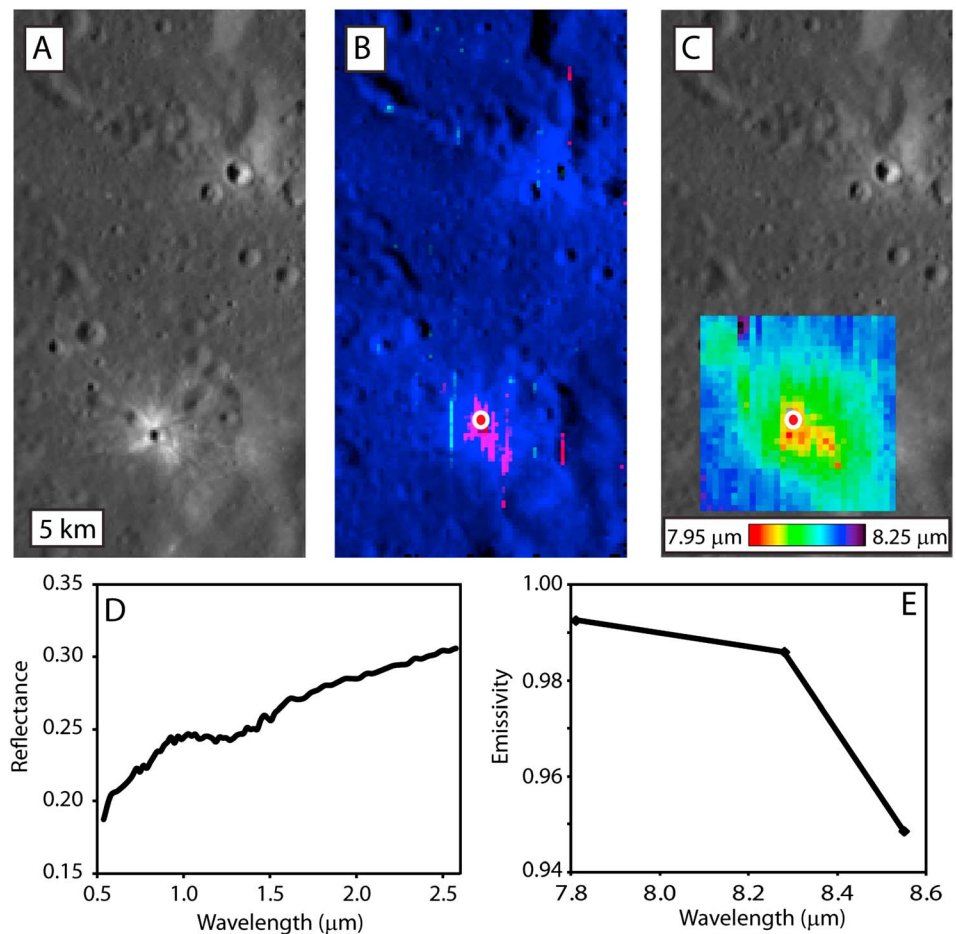


Figure 14. (a) LROC WAC albedo image of North Ray (8.8°S, 15.5°E) and South Ray (9.2°S, 15.4°E) craters. (b) M^3 Spectral parameter map of the same region, where red = 1.25 μm IBD, green = 1.00 μm IBD, and blue = 1.58 reflectance. The areas of pure crystalline plagioclase are red/pink in color. (c) Diviner CF map for South Ray crater. The areas with short CF values indicative of plagioclase are red in color. (d) M^3 reflectance spectrum of the high 1.25 μm IBD value region in the northwest ejecta blanket of South Ray as marked by the red dot in Figure 14b. (e) Diviner emissivity spectrum for the same region in the northwest ejecta blanket of South Ray crater.

plagioclase. Spectra extracted for a unit in the northwestern portion of the ejecta blanket from the M^3 reflectance data (Figure 14d) and the Diviner emissivity data (Figure 14e) confirm the presence of plagioclase. Similarly, good correlations are observed in the central peaks of Jackson and Humboldt craters. The distribution of units identified as spectrally pure plagioclase in M^3 reflectance data is similar to the distribution of units having Diviner CF values consistent with a plagioclase-dominated composition observed in Figures 15 and 16. Thus, the observations in both the NIR and TIR spectral ranges indicate regions dominated by a single-mineral phase, plagioclase, which can be further analyzed using the Diviner TIR data to estimate the composition of plagioclase (An#).

The plagioclase composition (An#) has been shown to be directly related to the wavelength position of the CF [Nash and Salisbury, 1991; Donaldson Hanna et al., 2012c]. Thus, the compositional variability of the plagioclase units observed in South Ray, Jackson, and Humboldt craters is estimated by calculating the median, average, and standard deviation of the Diviner CF values for all the pixels confirmed to be spectrally pure plagioclase. In addition, an average Diviner emissivity spectrum is calculated by taking the average and standard deviation emissivity value for each of the three spectral bands. In Figure 17, the histograms of all spectrally pure plagioclase pixels analyzed in South Ray, Jackson, and Humboldt craters are plotted along with the average emissivity spectra for each of the craters. The Y error bars on the average emissivity spectra are the standard deviations calculated from the mean for each Diviner spectral band. The histograms of spectrally pure plagioclase regions in the central peaks of Humboldt and Jackson are similar as their average

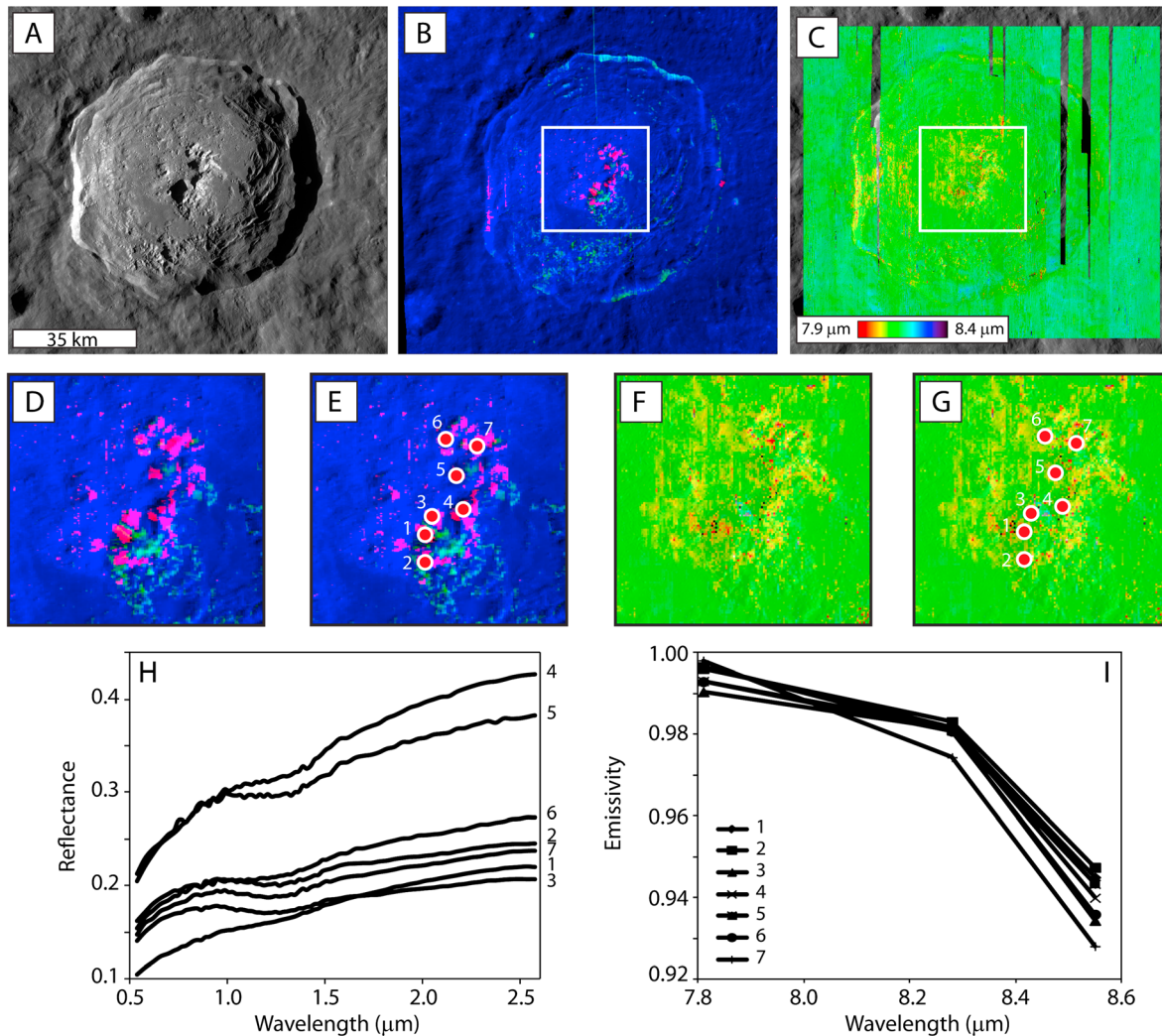


Figure 15. (a) LROC WAC albedo image of Jackson crater (22.063°N, 163.3255°W). (b) M^3 spectral parameter map of the same region, where red = 1.25 μm IBD, green = 1.00 μm IBD, and blue = 1.58 reflectance. The areas of pure crystalline plagioclase are red/pink in color. (c) Diviner CF map for Jackson crater. The areas with short CF values indicative of plagioclase are red in color. (d) M^3 spectral parameter map of the central peak structure of Jackson crater. (e) Spectral parameter map with red circles highlighting 5×5 pixel regions where spectra were extracted. (f) Diviner CF map of the central peak structure of Jackson crater. (g) Diviner CF map with red circles highlighting 3×3 pixel regions where spectra were extracted. (h) M^3 reflectance spectra of the high 1.25 μm IBD value regions in the central peak structure of Jackson as marked by the red dots in Figure 15d. (i) Diviner emissivity spectra for the same regions in the central peak structure of Jackson crater. The white boxes highlight the region examined in Figures 15d, 15e, 15f, and 15g.

CF values of $7.90 \pm 0.05 \mu\text{m}$ and $7.87 \pm 0.05 \mu\text{m}$. On the other hand, the CF values in the northwest ejecta blanket of South Ray crater are shifted to slightly longer values as the average CF value is $8.00 \pm 0.02 \mu\text{m}$. This is likely the result of minor amounts of mafic minerals mixed into the spectrally pure regions in the ejecta blanket, spatial mixing in the measured Diviner footprint with minor contributions from nonpure and/or noncrystalline anorthositic highland materials, and/or minor amounts of space weathering of the ejecta blanket. Within standard deviation, the spectral shape of the average spectrum from each crater is very similar. To better understand the compositional variability of plagioclase globally distributed across the lunar highlands, a histogram is calculated for all the pixels for spectrally pure plagioclase regions identified in all 37 highland craters. A single distribution of Diviner CF values is observed in the histogram (Figure 18) with a mean CF value of $7.91 \pm 0.05 \mu\text{m}$, suggesting that the average composition of plagioclase identified in all of the highlands craters is similar. Plagioclase composition is not the only factor in the width of the CF value distribution, as space weathering, topography, and/or minor contributions of mafic minerals can affect the CF value. The effect each has on the CF value will need to be investigated further in the future for more robust determinations of composition.

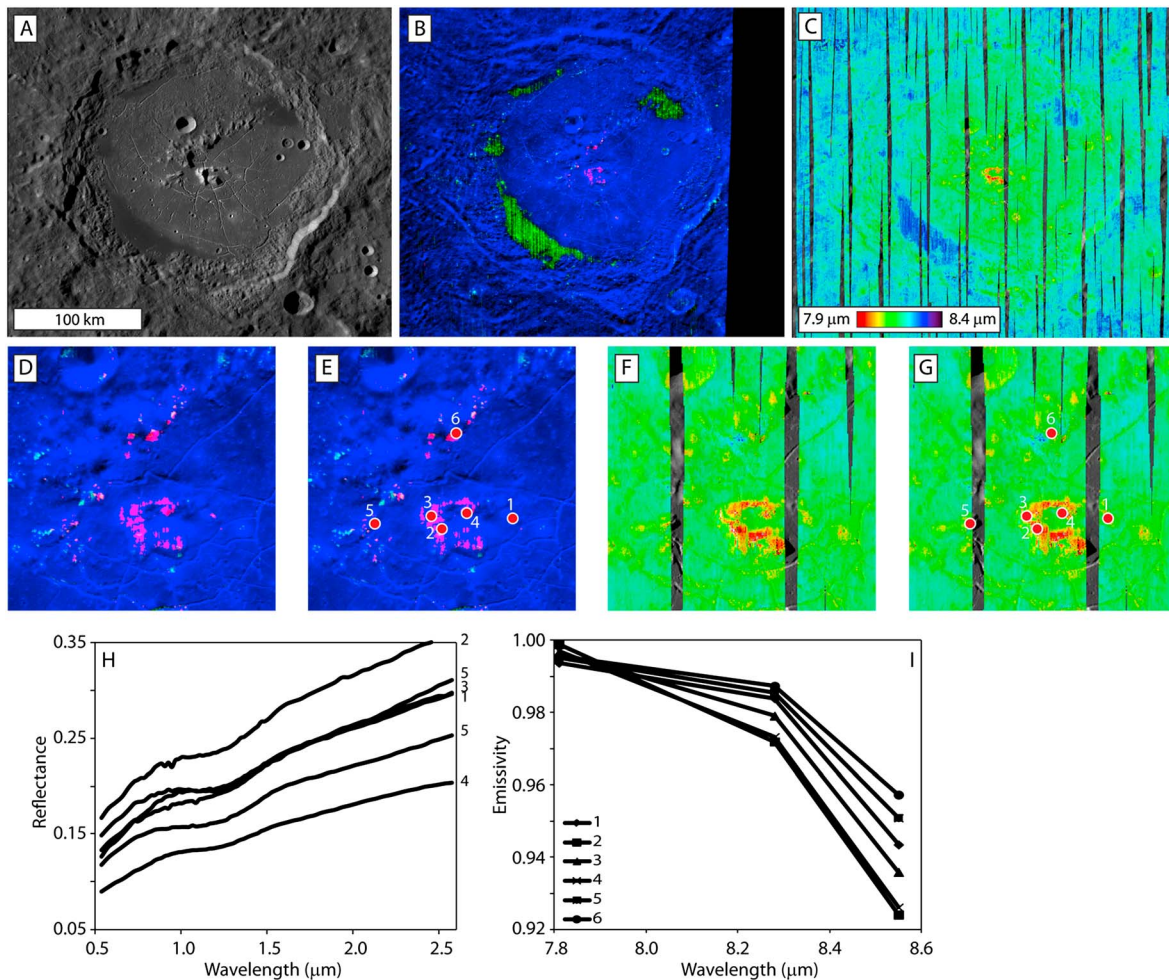


Figure 16. (a) LROC WAC albedo image of Humboldt crater (27.0858°S, 80.167°E). (b) M^3 spectral parameter map of the same region, where red = 1.25 μm IBD, green = 1.00 μm IBD, and blue = 1.58 reflectance. The areas of pure crystalline plagioclase are red/pink in color. (c) Diviner CF map for Humboldt crater. The areas with short CF values indicative of plagioclase are red in color. (d) M^3 spectral parameter map of the central peak structure of Humboldt. (e) Spectral parameter map with red circles highlighting 5×5 pixel regions where spectra were extracted. (f) Diviner CF map of the central peak structure of Humboldt. (g) Diviner CF map with red circles highlighting 3×3 pixel regions where spectra were extracted. (h) M^3 reflectance spectra of the high 1.25 μm IBD value regions in the central peak structure of Humboldt as marked by the red dots in Figure 16d. (i) Diviner emissivity spectra for the same regions in the central peak structure of Humboldt crater.

The mean Diviner CF value of $7.91 \pm 0.05 \mu\text{m}$ can be compared to the wavelength position of the CF of anorthite (An_{96}) measured under simulated lunar conditions in the laboratory to estimate the $An\#$ for the observed pure plagioclase units. The anorthite megacrysts were collected on two flow units, one unit dated from the July 1874 eruption on the NNE slope and an undated unit on the far east coast of the island of the Miyake-jima volcano [A. Petrov, unpublished data, 2014] and show little evidence for terrestrial weathering or contamination. The Miyake-jima anorthite was measured under simulated lunar conditions in the Simulated Lunar Environment Chamber at the University of Oxford [Thomas *et al.*, 2012]. Lunar conditions are simulated by evacuating the chamber to vacuum conditions (pressure $< 10^{-3}$ mbar), cooling the chamber to ~ 100 K using liquid nitrogen, heating the sample from below to 350 K, and heating the sample from above using a solar-like halogen lamp. Under these environmental conditions, the CF position of anorthite (An_{96}) was measured at $7.84 \pm 0.03 \mu\text{m}$. The mean CF value at $7.91 \pm 0.05 \mu\text{m}$ measured by Diviner suggests that the plagioclase composition across the highlands is relatively uniform in composition, highly calcium (An_{96}) and is consistent with plagioclase compositions found in the ferroan anorthosites (An_{94-98}) in the Apollo sample collection. Thus, the plagioclase composition measured in ferroan anorthosites is representative of plagioclase compositions throughout the lunar highlands. CF values $< 7.84 \mu\text{m}$ are observed in several craters like Jackson. While these pure plagioclase units are not the dominant type of plagioclase observed across the

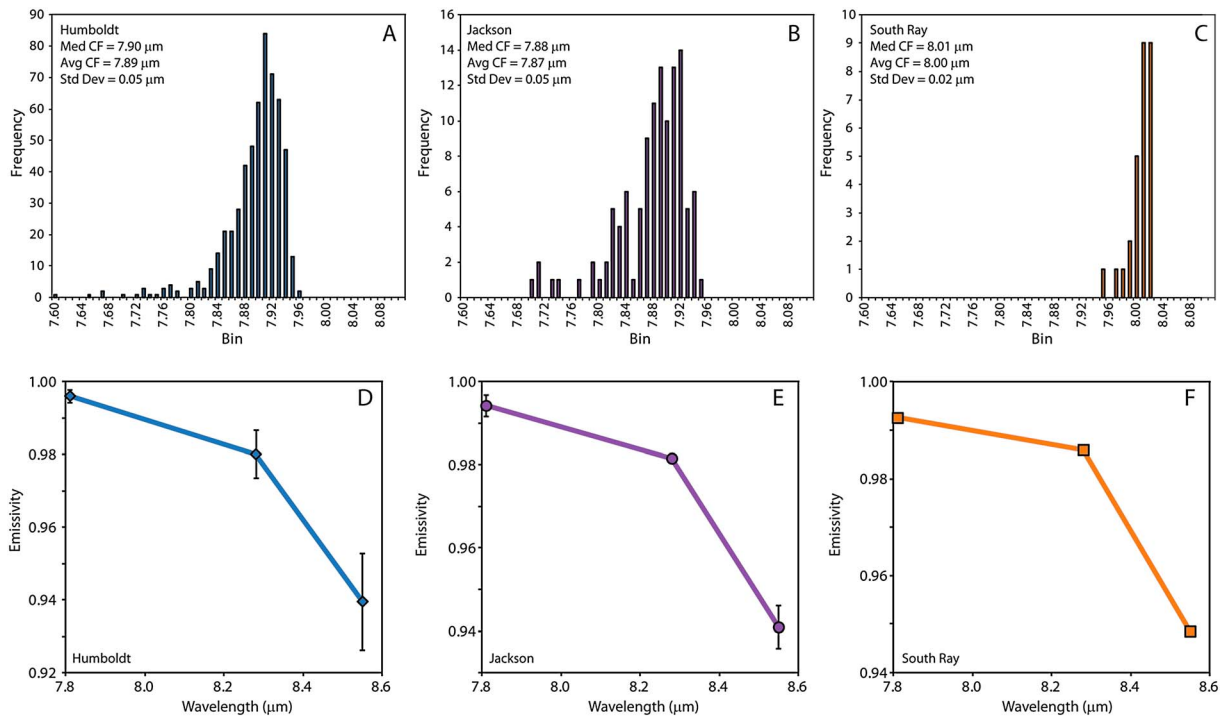


Figure 17. (a) Histogram of all the spectrally pure plagioclase pixels analyzed in Humboldt's central peak. (b) Histogram of all the spectrally pure plagioclase pixels analyzed in Jackson's central peak. (c) Histogram of all the spectrally pure plagioclase pixels analyzed in South Ray's northwest ejecta blanket. (d) Average Diviner emissivity spectrum for Humboldt crater. Y error bars are the standard deviations calculated from the mean for each Diviner spectral band. (e) Average Diviner emissivity spectrum for Jackson crater. (f) Average Diviner emissivity spectrum for South Ray crater.

lunar surface, these CF values could represent units that are more Na-rich or intermediate in composition and similar to the intermediate plagioclase units identified by *Greenhagen et al.* [2010]. Diviner CF values $>7.84 \mu\text{m}$ likely result from the contribution of minor amounts of mafic minerals (1–2 vol %) within the anorthosite, spatial mixing in the measured Diviner footprint with minor contributions from nonpure, and/or noncrystalline anorthositic highland materials or more mafic-rich materials and/or minor amounts of space weathering. Further investigation is necessary to determine the role of these factors on the wavelength position of the CF.

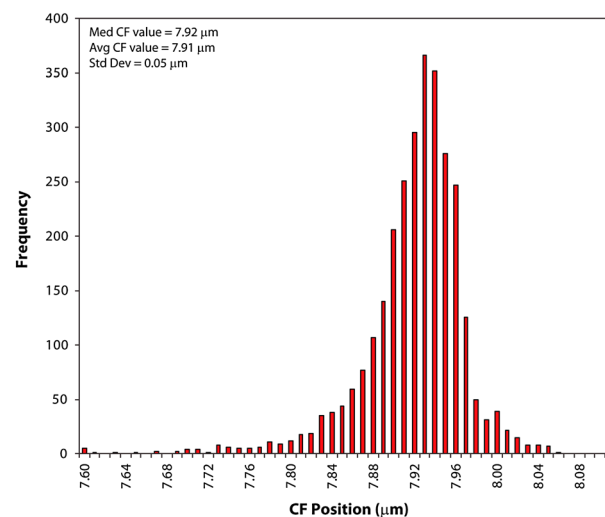


Figure 18. Histogram for all the spectrally pure plagioclase pixels analyzed in all of the 37 craters used in this compositional study. The histogram has a single distribution with a mean CF value of $7.91 \mu\text{m}$ and a standard deviation of $0.05 \mu\text{m}$.

5. Global Overview

Surface exposures of the anorthositic crust can be evaluated in the context of crustal thickness models to constrain the thickness of the original layer of anorthositic crust. All identified exposures of anorthosite are overlain on the GRAIL crustal thickness map [Wieczorek et al., 2012] in Figure 19. The ~650 targets evaluated are classified according to the character of their observed absorption features as described above and the inferred mineralogy. Anorthosite classes include (1) only pure anorthosite units are identified, (2) only nonpure anorthosite units are identified, (3) spatially separate units of pure anorthosite and nonpure

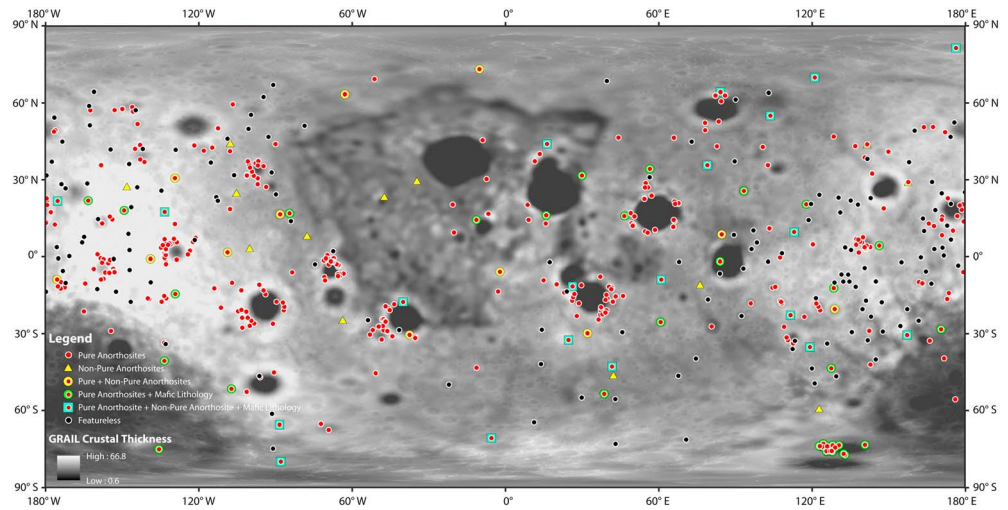


Figure 19. All the anorthosite identifications are overlain on the GRAIL crustal thickness map [Wieczorek *et al.*, 2012] and LROC WAC global mosaic. The red circles indicate craters where only pure anorthosite exposures ($\geq 99\%$ plagioclase) are identified. The yellow triangles indicate craters where only nonpure anorthosite exposures ($\leq 98\%$ plagioclase) are identified. The yellow circles with red circles in the center indicate craters with units of pure anorthosite and separate units of nonpure anorthosites. The green circles with red circles in the center indicate craters with units of pure anorthosite and separate units of mafic minerals. The cyan squares with red circles in the center indicate craters with units of pure anorthosite along with separate units of nonpure anorthosite and mafic minerals. The black and white circles indicate craters that had featureless spectra (i.e., no diagnostic mineral absorption near 1, 1.25, or $2\ \mu\text{m}$).

anorthosite are identified, (4) spatially separate units of pure anorthosite and mafic-rich lithologies are identified, and (5) spatially separate units of pure anorthosite, nonpure anorthosite, and mafic-rich lithologies are identified. Target areas that had no detectable absorption bands or featureless spectra are also included as some may indicate regions of “shocked” anorthosite.

Most of the regions identified as only pure anorthosite are from the walls and rims of simple craters (diameters $< 30\ \text{km}$) and are associated with the rings of multiring and peak ring basins. Other regions identified as only pure anorthosite are concentrated in the central peaks of complex craters between ~ 30 and $210\ \text{km}$ in diameter. Figures 10 and 11 provide good examples of the central peaks of Humboldt, Keeler, and Aitken craters, where only pure anorthosite was identified. Many of these pure anorthosite identifications reside in the feldspathic highlands terrane (FHT) [Jolliff *et al.*, 2000] and correlate to the thickest portions of the lunar crust as indicated by the GRAIL crustal thickness model in Figure 19. Crustal thickness values for all areas, where only pure anorthosite is identified, are extracted from the GRAIL model using the central latitude and longitude of the target areas. A histogram of the crustal thickness values for these pure anorthosite exposures is shown along with a histogram of the global crustal thickness values in Figure 20. The exposures of only pure anorthosite are observed at a range of crustal thicknesses from 9 to 63 km with a mean value of 42 km.

Regions where pure anorthosite is identified along with spatially separate nonpure anorthosite and/or mafic minerals are confined to the walls of a few simple craters (11–28 km in diameter) as seen in Proclus crater in Figure 12 and the central peaks of complex craters (37–185 km in diameter) as seen in Langrenus crater in Figure 13. These regions are identified in all three of the major crustal terranes: FHT, Procellarum KREEP terrane (PKT), and SPA [Jolliff *et al.*, 2000]. In Figure 20, a histogram of the crustal thickness values for regions that exhibit spatially separate units of pure anorthosite along with mafic-rich units are shown for comparison with the histograms of the global crustal thickness values and crustal thickness values for regions where only pure anorthosite is identified. The exposures of pure anorthosite plus some mafic lithology are observed at a range of crustal thicknesses from 9 to 54 km with a mean value of 34 km. The mean and distribution of crustal thickness values for regions of pure anorthosite plus some mafic lithology are clearly shifted to lower values than the mean and distribution of crustal values for regions of only pure anorthosite.

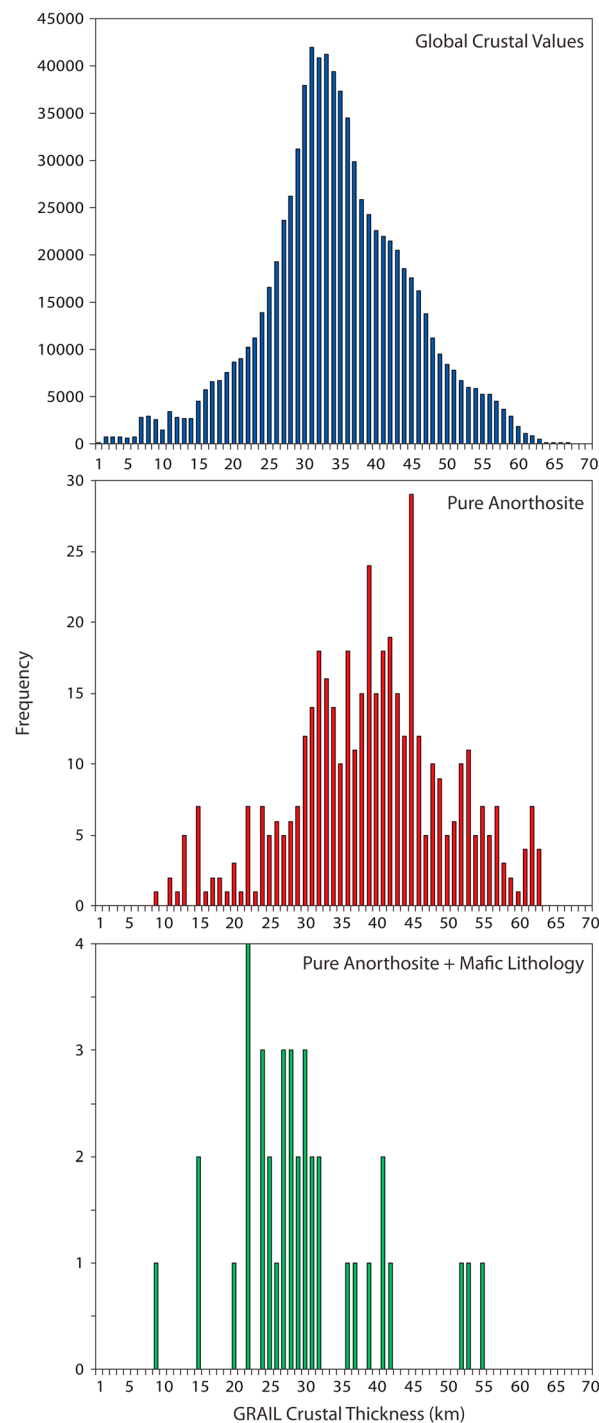


Figure 20. (top) Histogram of global crustal thickness values derived from an equal area projection of the GRAIL crustal thickness model [Wieczorek *et al.*, 2012]. (middle) Histogram of GRAIL crustal thickness values for target areas where only pure anorthosite units are identified. The red circles in Figure 19 identify target areas where only pure anorthosite is identified. (bottom). Histogram of GRAIL crustal thickness values for target areas where pure anorthosite units are identified along with mafic-rich units. The green circles with red circles in their center in Figure 19 identify these target areas. For the histograms in the middle and bottom plots, GRAIL crustal thickness values are extracted for each target area using the target's central latitude and longitude.

The lower boundary value for the thickness of the original pure anorthositic layer can be estimated by evaluating the crustal thickness values at which only pure anorthosite exposures are identified. The origin of the nonpure anorthosites and mafic lithologies observed along with pure anorthosite exposures is unknown and therefore ignored. These mafic-rich units could originate from (1) a more mafic-rich layer in the lower crust left over from the crystallization of the lunar magma ocean, (2) lower crustal plutons emplaced postmagma ocean, (3) impact melts emplaced during crater formation [e.g., Osinski *et al.*, 2011], and/or (4) mare contamination [Yamamoto *et al.*, 2012]. Most of the exposures of pure anorthosite associated with the exposures of nonpure anorthosites and/or mafic lithologies are concentrated at crustal thickness values between 22 and 32 km, while most exposures of only pure anorthosite are concentrated at crustal values between 30 and 63 km. Thus, a lower boundary value for the thickness of the original pure anorthositic layer in the crust can be estimated at approximately 30 km.

6. Discussion and Conclusions

The new high spectral and high spatial resolution data unambiguously confirm the presence of pure crystalline plagioclase based on the observed diagnostic absorption at $1.25\ \mu\text{m}$ due to Fe^{2+} in the crystal structure of plagioclase and allow the geologic context to be evaluated. Actual exposures of crystalline plagioclase are small in areal context. As seen in Figures 6 and 7, most of the exposures of pure crystalline plagioclase identified on the inner rings of Hertzprung and Nectaris basins are the walls of fresh, small craters ($<5\ \text{km}$). Additionally, the exposures of pure crystalline plagioclase in the central peaks of Keeler and Aitken craters as seen in Figure 11 are also on the order of $<5\ \text{km}$. None of these exposures of pure anorthosite would have been resolved in previous low spatial resolution data sets. Ohtake *et al.* [2009] demonstrated the effect of spatial resolution on pure plagioclase exposures on Orientale's Inner Rook. As the spatial resolution decreased, the depth of

the plagioclase absorption band decreased. Thus, the advent of combined high spatial and spectral resolution spectrometers that could produce data sets like those of M³, Spectral Profiler, and Multiband Imager have now only allowed for the detailed analysis done in this work.

These extended results now unambiguously identify pure crystalline plagioclase associated with the ring structures of most of the nearside and farside multiring and peak ring basins. This observation requires an extensive zone of highly pure ($\geq 99\%$ plagioclase), compositionally homogeneous anorthositic crust associated with each basin. These results corroborate results by Yamamoto *et al.* [2012] using the Spectral Profiler onboard SELENE. The occurrence of these basins randomly across the globe suggests that there exists a global layer of compositionally homogeneous anorthositic crust and supports the hypothesis that it formed from the crystallization of plagioclase within a magma ocean of global scope [e.g., Smith *et al.*, 1970; Wood *et al.*, 1970; Ryder, 1982; Warren, 1985, 1990]. The abundance, composition, and purity of anorthosite as determined by NIR and TIR spectroscopic analyses provide important constraints on lunar magma ocean models since they require a mechanism to efficiently remove crystallizing plagioclase from the remaining mafic liquid. Several mechanisms have been proposed for creating this highly pure portion of the lunar crust. Parmentier and Liang [2010] proposed that buoyantly driven melt migration could send the residual mafic liquid deeper and away from the crystallized plagioclase-rich solid located at the top of the magma ocean. Using the formation of the Sept Iles layered intrusion as an example, Namur *et al.* [2011] suggested that as the mafic lower crust crystallized in situ at the base of the magma ocean, the isolated plagioclase grains could have been removed and floated to the top of the magma ocean to crystallize and produce a layer of pure anorthositic crust. Modeling of crystal settling in the lunar magma ocean by Suckale *et al.* [2012] proposed that the late-stage floatation of plagioclase is related to the rate of crystal settling and the abundance of suspended crystals in the residual liquid.

After the solidification of the lunar magma ocean, basin- and crater-forming impacts modified the anorthositic crust by mixing, uplifting, ejecta redistribution, and gardening components. The analyses of multiring basins Orientale, Crisium, Humorum, and Nectaris suggested that during the basin-forming impact events, the upper crustal materials are sampled and uplifted in the inner ring [e.g., Spudis *et al.*, 1984; Pike and Spudis, 1987; Spudis, 1993; Cheek *et al.*, 2013]. Our observations suggest that this is true for all scales of basin-forming impacts, as the pure crystalline plagioclase is identified in the inner rings of peak- and multiring basins.

Our observations indicate that the locations where only pure anorthosite is identified are concentrated at crustal thickness values between 30 and 63 km, whereas locations where exposures of pure anorthosite also include some nearby mafic lithology are concentrated at lower crustal thickness values between 22 and 32 km (Figure 20). The concentration of exposures of only pure anorthosite at higher crustal values (30 to 63 km) has little to no overlap of crustal thicknesses for the exposures of pure anorthosite plus some mafic lithology. Although the origin of the mafic lithologies is not yet determined, it is clear that access to such mafic components requires thinner crust. Compositional analysis on these mafic units could help in further constraining their role in crustal evolution. Assuming that this concentration of pure anorthosite at high crustal thickness values is related to the primary anorthositic crust, then these data indicate the thickness of the original layer of anorthositic crust must have been at least 30 km thick.

Acknowledgments

Thank you to George Kramer and anonymous reviewers for their thoughtful comments as they improved this manuscript greatly. Many thanks to Francis McCubbin and Steve Elardo for sharing such beautiful anorthite samples with us. The authors also thank Noah Petro for processing and providing the LROC WAC mosaic. Support for this research through the NASA Lunar Science Institute at Brown University (grant ID NNA09DB34A) is gratefully acknowledged.

References

- Adams, J. B. (1974), Visible and near infrared diffuse reflectance spectra of pyroxenes as applied to remote sensing of solid objects in the solar system, *J. Geophys. Res.*, **79**, 4829–4836, doi:10.1029/JB079i032p04829.
- Adams, J. B., and L. H. Goulaud (1978), Plagioclase feldspars: Visible and near infrared diffuse reflectance spectra as applied to remote sensing, *Proc. Lunar Planet. Sci. Conf.*, **9**, 2901–2909.
- Adams, J. B., and T. B. McCord (1970), Remote sensing of lunar surface mineralogy: Implications from visible and near infrared reflectivity of Apollo 11 samples, *Geochim. Cosmochim. Acta*, **3**, 1937–1945.
- Adams, J. B., and T. B. McCord (1971a), Optical properties of mineral separates, glass, and anorthositic fragments from Apollo mare samples, *Proc. Lunar Planet. Sci. Conf.*, **2**, 117–133.
- Adams, J. B., and T. B. McCord (1971b), Alteration of lunar optical properties: Age and compositional effects, *Science*, **171**, 567–571.
- Adams, J. B., F. Hörz, and R. V. Gibbons (1979), Effects of shock-loading on the reflectance spectra of plagioclase, pyroxene, and glass, *Proc. Lunar Planet. Sci. Conf.*, **10**, 1–3.
- Allen, C. C., B. T. Greenhagen, K. L. Donaldson Hanna, and D. A. Paige (2012), Analysis of lunar pyroclastic deposit FeO abundances by LRO Diviner, *J. Geophys. Res.*, **117**, E00H28, doi:10.1029/2011JE003982.
- Amma-Miyasaka, M., and M. Nakagawa (2002), Origin of anorthite and olivine megacrysts in island-arc tholeiites: Petrological study of 1940 and 1962 ejecta from Miyake-jima volcano, Izu-Mariana arc, *J. Volcanol. Geotherm. Res.*, **117**, 263–283.

- Anderson, L. E., and E. A. Whitaker (1982), NASA catalogue of lunar nomenclature, NASA RP-1097.
- Baker, D. M. H., J. W. Head, G. A. Neumann, D. E. Smith, and M. T. Zuber (2012), The transition from complex craters to peak-ring basins on the Moon: New morphometric measurements from LOLA and LROC WAC data, *Proc. 2012 Lunar Science Forum*, 564.
- Bandfield, J. L., R. R. Ghent, A. R. Vasavada, D. A. Paige, S. J. Lawrence, and M. S. Robinson (2011), Lunar surface rock abundance and regolith fines temperatures derived from LRO Diviner Radiometer data, *J. Geophys. Res.*, **116**, E00H02, doi:10.1029/2011JE003866.
- Bell, P. M., and H. K. Mao (1973), Optical and chemical analyses of iron in Lunar 20 plagioclase, *Geochim. Cosmochim. Acta*, **37**, 755–759.
- Blewett, D. T., P. G. Lucey, B. R. Hawke, and B. L. Jolliff (1997), Clementine images of the lunar sample-return stations: Refinement of FeO and TiO₂ mapping techniques, *J. Geophys. Res.*, **102**, 16,319–16,325, doi:10.1029/97JE01505.
- Blue, J. (2004), Gazetteer of Planetary Nomenclature. [Available at <http://planetarynames.wr.usgs.gov/>, accessed January 2004.]
- Boardman, J. W., C. M. Pieters, R. O. Green, S. R. Lundeen, P. Varanasi, J. Nettles, N. Petro, P. Isaacson, S. Besse, and L. A. Taylor (2011), Measuring moonlight: An overview of the spatial properties, lunar coverage, selenolocation, and related Level 1B products of the Moon Mineralogy Mapper, *J. Geophys. Res.*, **116**, E00G14, doi:10.1029/2010JE003730.
- Bruckenthal, E. A., and C. M. Pieters (1984), Spectral effects of natural shock on plagioclase feldspar, *Proc. Lunar Planet. Sci. Conf.*, **15**, 96–97.
- Burns, R. G. (1970), *Mineralogical Applications of Crystal-Field Theory*, pp. 1–224, Cambridge Univ. Press, London.
- Burns, R. G. (1993), *Mineralogical Applications of Crystal-Field Theory*, 2nd ed., 575 pp., Cambridge Univ. Press, Cambridge, U. K.
- Bussey, D. B. J., and P. D. Spudis (2000), Compositional studies of the Orientale, Humorum, Nectaris, and Crisium lunar basins, *J. Geophys. Res.*, **105**, 4235–4243, doi:10.1029/1999JE001130.
- Cheek, L. C., and C. M. Pieters (2012), Variations in anorthosite purity at Tsiolkovsky crater on the Moon, *Proc. Lunar Planet. Sci. Conf.*, **43**, 2624.
- Cheek, L. C., C. M. Pieters, M. D. Dyar, and K. A. Milam (2009), Revisiting plagioclase optical properties for lunar exploration, *Proc. Lunar Planet. Sci. Conf.*, **40**, 1928.
- Cheek, L. C., C. M. Pieters, S. W. Parman, M. D. Dyar, E. A. Speicher, and R. F. Cooper (2011), Spectral characteristics of plagioclase with variable iron content: Applications to remote sensing of the lunar crust, *Proc. Lunar Planet. Sci. Conf.*, **42**, 1617.
- Cheek, L. C., K. L. Donaldson Hanna, C. M. Pieters, J. W. Head, and J. L. Whitten (2013), The distribution and purity of anorthosite across the Orientale Basin: New perspectives from Moon Mineralogy Mapper Data, *J. Geophys. Res. Planets*, **118**, 1805–1820, doi:10.1002/jgre.20126.
- Conel, J. E. (1969), Infrared emissivities of silicates: Experimental results and a cloudy atmospheric model of spectral emission from condensed particulate mediums, *J. Geophys. Res.*, **74**, 1614–1634, doi:10.1029/JB074i006p01614.
- Coombs, C. R., B. R. Hawke, P. G. Lucey, P. D. Owensby, and S. H. Zisk (1990), The Alphonsus region: A geologic and remote-sensing perspective, *Proc. Lunar Planet. Sci. Conf.*, **20**, 161–174.
- Cooper, B. L., J. W. Salisbury, R. M. Killen, and A. E. Potter (2002), Mid infrared spectra features and their powders, *J. Geophys. Res.*, **107**(E4), 5017, doi:10.1029/2000JE001462.
- de Hon, R. A. (1979), Structural model of the Imbrium basin, *Proc. Lunar Planet. Sci. Conf.*, **10**, 271–273.
- Dhingra, D., C. M. Pieters, J. W. Boardman, J. W. Head, P. J. Isaacson, and L. A. Taylor (2011), Compositional diversity at Theophilus crater: Understanding the geologic context of Mg-spinel bearing central peaks, *Geophys. Res. Lett.*, **38**, L11201, doi:10.1029/2011GL047314.
- Donaldson Hanna, K. L., L. C. Cheek, C. M. Pieters, J. F. Mustard, M. B. Wyatt, and B. T. Greenhagen (2012a), Global identifications of crystalline plagioclase across the lunar surface using M³ and Diviner data, *Proc. Lunar Planet. Sci. Conf.*, **43**, 1968.
- Donaldson Hanna, K. L., M. B. Wyatt, I. R. Thomas, N. E. Bowles, B. T. Greenhagen, A. Maturilli, J. Helbert, and D. A. Paige (2012b), Thermal infrared emissivity measurements under a simulated lunar environment: Application to the Diviner Lunar Radiometer Experiment, *J. Geophys. Res.*, **117**, E00H05, doi:10.1029/2011JE003862.
- Donaldson Hanna, K. L., I. R. Thomas, N. E. Bowles, B. T. Greenhagen, C. M. Pieters, J. F. Mustard, C. R. M. Jackson, and M. B. Wyatt (2012c), Laboratory emissivity measurements of the plagioclase solid solution series under varying environmental conditions, *J. Geophys. Res.*, **117**, E11004, doi:10.1029/2012JE004184.
- Dowty, E., M. Prinz, and K. Keil (1974), Ferroan anorthosite: A widespread and distinctive lunar rock type, *Earth Planet. Sci. Lett.*, **24**, 15–25.
- Fassett, C. I., J. W. Head III, S. J. Kadish, E. Mazarico, G. A. Neumann, D. E. Smith, and M. T. Zuber (2012), Lunar impact basins: Stratigraphy, sequence and ages from superposed impact crater populations measured from Lunar Orbiter Laser Altimeter (LOLA) data, *J. Geophys. Res.*, **117**, E00H06, doi:10.1029/2011JE003951.
- Gibbons, R. V., and T. J. Ahrens (1977), Effects of shock pressures on calcic plagioclase, *Phys. Chem. Miner.*, **1**, 95–107.
- Glotch, T. D., et al. (2010), Highly silicic compositions on the Moon, *Science*, **329**, 1510–1513.
- Green, R. O., et al. (2011), The Moon Mineralogy Mapper (M³) imaging spectrometer for lunar science: Instrument description, calibration, on-orbit measurements, science data calibration and on-orbit validation, *J. Geophys. Res.*, **116**, E00G19, doi:10.1029/2011JE003797.
- Greenhagen, B. T. (2009), Thermal emission remote sensing of the Moon: Design and development of Diviner Lunar Radiometer compositional capabilities, PhD dissertation, Univ. of Calif., Los Angeles, Calif.
- Greenhagen, B. T., et al. (2010), Global silicate mineralogy from the Diviner Lunar Radiometer, *Science*, **329**, 1507–1509, doi:10.1126/science.1192196.
- Greenhagen, B. T., P. G. Lucey, J. L. Bandfield, P. O. Hayne, J. P. Williams, and D. A. Paige (2011), The Diviner Lunar Radiometer compositional data products: Description and examples, *Proc. Lunar Planet. Sci. Conf.*, **42**, 2679.
- Gross, J., A. H. Treiman, and C. Mercer (2012), Sinking the lunar magma ocean: New evidence from meteorites and the return of serial magmatism, *Proc. Lunar Planet. Sci. Conf.*, **43**, 2306.
- Hapke, B. (2001), Space weathering from Mercury to the asteroid belt, *J. Geophys. Res.*, **106**(E5), 10,039–10,073, doi:10.1029/2000JE001338.
- Hawke, B. R., P. G. Lucey, J. F. Bell, and P. D. Owensby (1985), Spectral studies of the highlands around the Nectaris Basin: Preliminary results, *Proc. Lunar Planet. Sci. Conf.*, **16**, 329–330.
- Hawke, B. R., C. A. Peterson, P. G. Lucey, G. J. Taylor, J. F. Bell, D. Blewett, and B. Campbell (1991), Remote sensing studies of the terrain northwest of Humorum basin, *Proc. Lunar Planet. Sci. Conf.*, **22**, 539–540.
- Hawke, B. R., C. A. Peterson, D. T. Blewett, D. B. J. Bussey, P. G. Lucey, G. J. Taylor, and P. D. Spudis (2003), Distribution and modes of occurrence of lunar anorthosite, *J. Geophys. Res.*, **108**(E6), 5050, doi:10.1029/2002JE001890.
- Hazen, R. M., P. M. Bell, and H. K. Mao (1978), Effects of compositional variation on absorption spectra of lunar pyroxenes, *Proc. Lunar Planet. Sci. Conf.*, **9**, 2919–2934.
- Head, J. W., C. I. Fassett, S. J. Kadish, D. E. Smith, M. T. Zuber, G. A. Neumann, and E. Mazarico (2010), Global distribution of large lunar craters: Implications for resurfacing and impactor populations, *Science*, **329**, doi:10.1126/science.1195050.
- Henderson, B. G., P. G. Lucey, and B. M. Jakosky (1996), New laboratory measurements of mid-IR emission spectra of simulated planetary surfaces, *J. Geophys. Res.*, **101**, 14,969–14,975, doi:10.1029/96JE01089.
- Hörz, F., and W. L. Quaide (1973), Debye-Scherrer investigations of experimentally shocked silicates, *Moon*, **6**, 45–82.

- Isaacson, P. J., A. Basu Sarbadhikari, C. M. Pieters, R. L. Klima, T. Hiroi, Y. Liu, and L. A. Taylor (2011), The Lunar Rock and Mineral Characterization Consortium: Deconstruction and integrated mineralogical, petrologic, and spectroscopic analyses of mare basalts, *Meteorit. Planet. Sci.*, *46*, 228–251, doi:10.1111/j.1945-5100.2010.01148.x.
- Isaacson, P. J., et al. (2013), Development, importance, and effect of a ground truth correction for the Moon Mineralogy Mapper reflectance data set, *J. Geophys. Res. Planets*, *118*, 369–381, doi:10.1002/jgre.20048.
- James, O. B., M. M. Lindstrom, and M. K. Flohr (1989), Ferroan anorthosite from lunar breccia 64435: Implications for the origin and history of lunar ferroan anorthosites, *Proc. Lunar Planet. Sci. Conf.*, *19*, 219–243.
- Johnson, J. R., and F. Hörz (2003), Visible/near-infrared spectra of experimentally shocked plagioclase feldspars, *J. Geophys. Res.*, *108*(E11), 5120, doi:10.1029/2003JE002127.
- Jolliff, B. L., J. J. Gillis, L. A. Haskin, R. L. Korotev, and M. A. Wieczorek (2000), Major lunar crustal terranes: Surface expressions and crust-mantle origins, *J. Geophys. Res.*, *105*(E2), 4197–4216, doi:10.1029/1999JE001103.
- Kato, M., S. Sasaki, K. Tanaka, Y. Iijima, and Y. Takizawa (2008), The Japanese lunar mission SELENE: Science goals and present status, *Adv. Space Res.*, *42*, 294–300.
- Keller, L. P., and D. S. McKay (1997), The nature and origin of rims on lunar soil grains, *Geochim. Cosmochim. Acta*, *61*, 2331–2341.
- Keller, L. P., S. J. Wentworth, and D. S. McKay (1998), Space weathering: Reflectance spectroscopy and TEM analysis of individual lunar soil grains, *Proc. Lunar Planet. Sci. Conf.*, *29*, 1762.
- Kimata, M., N. Nishida, M. Shimizu, S. Saito, T. Matsui, and Y. Arakawa (1995), Anorthite megacrysts from island arc basalts, *Mineral. Mag.*, *59*, 1–14.
- Klima, R. L., C. M. Pieters, and M. D. Dyar (2007), Spectroscopy of synthetic Mg-Fe pyroxenes I: Spin-allowed and spin-forbidden crystal field bands in the visible and near-infrared, *Met. Planet. Sci.*, *42*, 235–253.
- Klima, R. L., C. M. Pieters, and M. D. Dyar (2008), Characterization of the 1.2 mm M1 pyroxene band: Extracting cooling history from near-IR spectra of pyroxenes and pyroxene-dominated rocks, *Met. Planet. Sci.*, *43*, 1591–1604.
- Klima, R. L., M. Darby, and C. M. Pieters (2011), Near-infrared spectra of clinopyroxenes: Effects of calcium content and crystal structure, *Meteorit. Planet. Sci.*, *46*, 379–395, doi:10.1111/j.1945-5100.2010.01158.x.
- Korotev, R. L., B. L. Jolliff, R. A. Zeigler, J. J. Gillis, and L. A. Haskin (2003), Feldspathic lunar meteorites and their implications for compositional remote sensing of the lunar surface and the composition of the lunar crust, *Geochim. Cosmochim. Acta*, *67*, 4895–4923.
- Kramer, G. Y., D. A. Kring, A. L. Nahm, and C. M. Pieters (2013), Spectral and photogeologic mapping of Schrödinger Basin and implications for post-South Pole-Aitken impact deep subsurface stratigraphy, *Icarus*, *223*, 131–148, doi:10.1016/j.icarus.2012.11.008.
- Logan, L. M., G. R. Hunt, J. W. Salisbury, and S. R. Balsamo (1973), Compositional implications of Christiansen frequency maximums for infrared remote sensing applications, *J. Geophys. Res.*, *78*, 4983–5003, doi:10.1029/JB078i023p04983.
- Longhi, J. (2003), A new view of lunar ferroan anorthosites: Postmagma ocean petrogenesis, *J. Geophys. Res.*, *108*(E8), 5083, doi:10.1029/2002JE001941.
- Longhi, J., and L. D. Ashwal (1985), Two-stage models for lunar and terrestrial anorthosites: Petrogenesis without a magma ocean, *J. Geophys. Res.*, *90*, C571–C584, doi:10.1029/JB090iS02p0C571.
- Lucey, P. G. (2002), Radiative transfer model constraints on the shock state of remotely sensed lunar anorthosites, *Geophys. Res. Lett.*, *29*(10), 1486, doi:10.1029/2001GL014655.
- Lucey, P. G., G. J. Taylor, and E. Malaré (1995), Abundance and distribution of iron on the Moon, *Science*, *268*, 1150–1153.
- Lucey, P. G., D. T. Blewett, and B. R. Hawke (1998), Mapping the FeO and TiO₂ content of the lunar surface with multispectral imagery, *J. Geophys. Res.*, *103*, 3679–3699, doi:10.1029/97JE03019.
- Lucey, P. G., D. A. Paige, B. T. Greenhagen, J. L. Bandfield, and T. D. Glotch (2010), Comparison of Diviner Christiansen Feature position and visible albedo: Composition and space weathering implications, *Proc. Lunar Planet. Sci.*, *41*, 1600.
- Lucey, P. G., E. Song, B. T. Greenhagen, J. Gillis-Davis, I. Thomas, N. Bowles, L. F. Millan, K. L. Donaldson Hanna, and D. A. Paige (2013), Global Diviner Christiansen Feature space weathering effects: Hypotheses, experiment, and mitigation, *Proc. Lunar Planet. Sci. Conf.*, *44*, 2890.
- Lundeen, S., S. McLaughlin, and R. Alanis (2011), Moon Mineralogy Mapper data product software interface specification, PDS document Version 9.10, Jet Propulsion Laboratory, JPL D-39032, Pasadena, Calif.
- Lyon, R. J. P. (1964), Evaluation of infrared spectrophotometry for compositional analysis of lunar and planetary soils, part II, Rough and powdered surfaces, *NASA Rep. CR-100*, 264 pp.
- Matsunaga, T., et al. (2008), Discoveries on the lithology of lunar crater central peaks by SELENE Spectral Profiler, *Geophys. Res. Lett.*, *35*, L23201, doi:10.1029/2008GL035868.
- McGee, J. J. (1993), Lunar ferroan anorthosites: Mineralogy, compositional variations, and petrogenesis, *J. Geophys. Res.*, *98*, 9089–9105, doi:10.1029/93JE00400.
- Namur, O., B. Charlier, C. Pirard, J. Hermann, J.-P. Liégeois, and J. V. Auwera (2011), Anorthosite formation by plagioclase flotation in ferrobasalt and implications for the lunar crust, *Geochim. Cosmochim. Acta*, *75*, 4998–5018.
- Nash, D. B., and J. W. Salisbury (1991), Infrared reflectance spectra (2.2–15 μ m) of plagioclase feldspars, *Geophys. Res. Lett.*, *18*, 1151–1154, doi:10.1029/91GL01008.
- Noble, S. K., C. M. Pieters, L. A. Taylor, R. V. Morris, C. C. Allen, D. S. McKay, and L. P. Keller (2001), The optical properties of the finest fraction of lunar soil: Implications for space weathering, *Meteorit. Planet. Sci.*, *36*, 31–42.
- Ohtake, M., J. Haruyama, T. Matsunaga, Y. Yokota, T. Morota, C. Honda, and LISM team (2008), Performance and scientific objectives of the SELENE (KAGUYA) Multiband Imager, *Earth Planets Space*, *60*, 257–264.
- Ohtake, M., et al. (2009), The global distribution of pure anorthosite on the Moon, *Nature*, *461*, doi:10.1038/nature08317.
- Ohtake, M., et al. (2012), Asymmetric crustal growth on the Moon indicated by primitive farside high materials, *Nat. Geosci.*, *5*(6), 384–388, doi:10.1038/NGEO1458.
- Ohtake, M., et al. (2013), One Moon, Many Measurements 3: Spectral reflectance, *Icarus*, *226*, 364–374.
- Osinski, G. R., L. L. Tornabene, and R. A. F. Grieve (2011), Impact ejecta emplacement on terrestrial planets, *Earth Planet. Sci. Lett.*, *310*, 167–181.
- Paige, D. A., et al. (2009), The Lunar Reconnaissance Orbiter Diviner Lunar Radiometer Experiment, *Space Sci. Rev.*, *150*, 125–160, doi:10.1007/s11214-009-9529-2.
- Paige, D. A., et al. (2010), Diviner Lunar Radiometer observations of cold traps in the Moon's south polar region, *Science*, *330*, 479–482, doi:10.1126/science.1187726.
- Papike, J. J., G. Ryder, and C. K. Shearer (1996), Lunar Samples, in *Planetary Materials, Reviews in Mineralogy*, vol. 36, edited by J. J. Papike, pp. 5–01–5–234, Mineralogical Society of America, Washington, D. C.
- Parmentier, E. M., and Y. Liang (2010), Formation of pure anorthosite during lunar magma ocean solidification: Implications for the melt-solid segregation process, *Proc. Lunar Planet. Sci. Conf.*, *41*, 1824.

- Peterson, C. A., B. R. Hawke, P. G. Lucey, C. R. Coombs, and P. D. Spudis (1995), Spectral reflectance studies of the Grimaldi region of the Moon, *Geophys. Res. Lett.*, **22**, 3055–3058, doi:10.1029/95GL02798.
- Peterson, C. A., B. R. Hawke, P. G. Lucey, G. J. Taylor, D. T. Blewett, and P. D. Spudis (1996), Anorthosite on the lunar nearside and farside, *Proc. Lunar Planet. Sci. Conf.*, **27**, 1025–1026.
- Peterson, C. A., B. R. Hawke, P. G. Lucey, G. J. Taylor, D. T. Blewett, and P. D. Spudis (1997), Lunar anorthosite: Identification and distribution of remnants of the primordial crust, *Proc. Lunar Planet. Sci. Conf.*, **28**, 1608.
- Pieters, C. M. (1986), Composition of the lunar highland crust from near-infrared spectroscopy, *Rev. Geophys.*, **24**, 557–578, doi:10.1029/RG024i003p00557.
- Pieters, C. M. (1996), Plagioclase and maskelynite diagnostic features, *Proc. Lunar Planet. Sci. Conf.*, **27**, 1031–1032.
- Pieters, C. M., E. M. Fischer, O. Rode, and A. Basu (1993), Optical effects of space weathering: The role of the finest fraction, *J. Geophys. Res.*, **98**, 20,817–20,824, doi:10.1029/93JE02467.
- Pieters, C. M., L. A. Taylor, S. K. Noble, L. P. Keller, B. Hapke, R. V. Morris, C. C. Allen, D. S. McKay, and S. Wentworth (2000), Space weathering on airless bodies: Resolving a mystery with lunar samples, *Meteorit. Planet. Sci.*, **35**, 1101–1107.
- Pieters, C. M., et al. (2009a), Mineralogy of the lunar crust in spatial context: First results from the Moon Mineralogy Mapper (M^3), *Proc. Lunar Planet. Sci. Conf.*, **40**, 2052.
- Pieters, C. M., et al. (2009b), The Moon Mineralogy Mapper (M1) on Chandrayaan-1, *Curr. Sci.*, **96**, 500–505.
- Pike, R. J., and P. D. Spudis (1987), Basin-ring spacing on the Moon, Mercury, and Mars, *Earth Moon Planets*, **39**, 129–194.
- Robinson, M. S., et al. (2010), Lunar Reconnaissance Orbiter Camera (LROC) Instrument Overview, *Space Sci. Rev.*, **150**, 81–124, doi:10.1007/s11214-010-9634-2.
- Ryder, G. (1982), Lunar anorthosite 60025, the petrogenesis of lunar anorthosites, and the composition of the Moon, *Geochim. Cosmochim. Acta*, **46**, 1591–1601.
- Salisbury, J. W., and L. S. Walter (1989), Thermal infrared (2.5 – 13.5 μm) spectroscopic remote sensing of igneous rock types on particulate planetary surfaces, *J. Geophys. Res.*, **94**, 9192–9202, doi:10.1029/JB094iB07p09192.
- Smith, J. V., A. T. Anderson, R. C. Newton, E. J. Olsen, and P. J. Wylie (1970), A petrologic model for the Moon based on petrogenesis, experimental petrology, and physical properties, *Geology*, **78**, 381–405.
- Smith, D. E., et al. (2010), Initial observations from the Lunar Orbiter Laser Altimeter (LOLA), *Geophys. Res. Lett.*, **37**, L18204, doi:10.1029/2010GL043751.
- Spudis, P. D. (1993), *The Geology of Multi-Ring Impact Basins*, 277 pp., Cambridge Univ. Press, Cambridge, U. K.
- Spudis, P. D., B. R. Hawke, and P. Lucey (1984), Composition of Orientale basin deposits and implications for the lunar basin-forming process, *J. Geophys. Res.*, **89**, C197–210, doi:10.1029/JB089iS01p0C197.
- Stöffler, D. (1971), Progressive metamorphism and classification of shocked and brecciated crystalline rocks at impact craters, *J. Geophys. Res.*, **76**, 5541–5551, doi:10.1029/JB076i023p05541.
- Suckale, J., L. T. Elkins-Tanton, and J. A. Sethian (2012), Crystals stirred up: 2. Numerical insights into the formation of the earliest crust on the Moon, *J. Geophys. Res.*, **117**, E08005, doi:10.1029/2012JE004067.
- Sunshine, J. M., and C. M. Pieters (1998), Determining the composition of olivine from reflectance spectroscopy, *J. Geophys. Res.*, **103**, 13,675–13,688, doi:10.1029/98JE01217.
- Takeda, H., A. Yamaguchi, D. D. Bogard, Y. Karouji, M. Ebihara, M. Ohtake, K. Saiki, and T. Arai (2006), Magnesian anorthosites and a deep crustal rock from the farside crust of the Moon, *Earth Planet. Sci. Lett.*, **247**, 171–184.
- Thomas, I. R., B. T. Greenhagen, N. E. Bowles, K. L. Donaldson Hanna, J. Temple, and S. B. Calcutt (2012), A new experimental setup for making thermal emission measurements in a simulated lunar environment, *Rev. Sci. Instrum.*, **83**, 124502, doi:10.1063/1.4769084.
- Tompkins, S., and C. M. Pieters (1999), Mineralogy of the lunar crust: Results from Clementine, *Met. Planet. Sci.*, **34**, 25–41.
- Vasavada, A. R., J. L. Bandfield, B. T. Greenhagen, P. O. Hayne, M. A. Seigler, J.-P. Williams, and D. A. Paige (2012), Lunar equatorial surface temperatures and regolith properties from the Diviner Lunar Radiometer Experiment, *J. Geophys. Res.*, **117**, E00H18, doi:10.1029/2011JE003987.
- von Engelhardt, W., and D. Stöffler (1968), Stages of shock metamorphism in crystalline rocks of the Ries basin, Germany, in *Shock Metamorphism of Natural Materials*, edited by B. M. French and N. M. Short, pp. 159–168, Mono Book Corp., Baltimore, Md.
- von Engelhardt, W., J. Arndt, D. Stöffler, W. R. Müller, H. Jeziorowski, and R. A. Gubser (1967), Diaplektische Gläser in den Breccien des Ries von Nördlingen als Anzeichen für Stosswellenmetamorphose, *Contrib. Mineral. Petrol.*, **15**, 91.
- Warren, P. H. (1985), The magma ocean concept and lunar evolution, *Ann. Rev. Earth Planet. Sci.*, **13**, 201–240.
- Warren, P. H. (1990), Lunar anorthosites and the magma-ocean plagioclase-flotation hypothesis: Importance of FeO enrichment in the parent magma, *Am. Mineral.*, **75**, 46–58.
- Wetherill, G. W. (1975), Possible slow accretion of the Moon and its thermal and petrological consequences, in *Papers Presented to the Conference on Origins of Mare Basalts and Their Implications for Lunar Evolution*, pp. 184–189, Lunar Science Institute, Houston, Tex.
- Wieczorek, M. A., et al. (2012), The crust of the Moon as seen by GRAIL, *Science*, **339**, 671–675, doi:10.1126/science.1231530.
- Wood, J. A., J. S. Dickey, U. B. Marvin, and B. N. Powell (1970), Lunar anorthosites and a geophysical model of the Moon, *Proc. Apollo 11 Lunar Sci. Conf.*, **1**, 965–988.
- Yamamoto, S., et al. (2012), Massive layer of pure anorthosite on the Moon, *Geophys. Res. Lett.*, **39**, L13201, doi:10.1029/2012GL052098.